

THESIS FOR THE DEGREE OF DOCTOR OF PHILOSOPHY

Atoms in Lithiated Carbon Fibres

MARCUS JOHANSEN

Department of Industrial and Materials Science
CHALMERS UNIVERSITY OF TECHNOLOGY
Gothenburg, Sweden 2023

Atoms in Lithiated Carbon Fibres

MARCUS JOHANSEN

ISBN 978-91-7905-916-3

© MARCUS JOHANSEN, 2023

Doktorsavhandlingar vid Chalmers tekniska högskola

Ny serie nr 5382

ISSN 0346-718X

Department of Industrial and Materials Science

Chalmers University of Technology

SE-412 69 Gothenburg

Sweden

Telephone: +46 (0)31-772 1000

Cover:

Illustration of electric transportation, schematic of a structural battery, representation of electron spectroscopy results from carbon fibres, and reconstruction of the distribution of atoms in lithiated carbon fibres based on atom probe tomography. Black dots represent carbon, red oxygen, blue nitrogen, and green lithium. The inset is an illustration of nearest neighbour analysis of lithium and nitrogen.

Printed by Chalmers Reproservice

Gothenburg, Sweden 2023

Abstract

Carbon fibres are key constituents of structural batteries, in which electrochemical energy storage and mechanical load bearing are merged in one multifunctional device. Here carbon fibres simultaneously act as structural reinforcement by carrying load and as battery electrode by hosting lithium (Li)-ions in its microstructure. However, conventional carbon fibres are not designed to be multifunctional. To enable carbon fibres with optimised multifunctional capabilities, a fundamental understanding of their microstructure, chemical information and interaction with Li is required.

In this thesis, mass spectrometry and electron spectroscopy techniques are developed and used to elucidate the atomic distribution, configuration, and interaction in commercial carbon fibres used in structural batteries. Here the methodology of analysing Li in carbon fibres with atom probe tomography (APT) and Auger electron spectroscopy (AES) is demonstrated. Synchrotron-based hard X-ray photoelectron spectroscopy (HAXPES) reveals that certain chemical states of N heteroatoms, pyridinic and pyrrolic, are connected to enhanced electrochemical performance of carbon fibres. AES shows that: Li distributes throughout the entire carbon fibre; the amount of trapped Li is higher and concentrated towards the centre of the fibre at increased discharge rates; Li is initially inserted in amorphous domains and with increased states of lithiation in crystalline domains; and Li plating can occur on individual fibres without spreading to adjacent fibres. APT on lithiated carbon fibres shows that: the distribution of Li is independent of the distribution of N heteroatoms; trapped Li is distributed uniformly in all domains; and Li agglomerates at elevated states of lithiation.

The work presented in this thesis paves the way for analysis of carbon-based battery materials with APT and AES. Furthermore, the work unveils much of the interplay between carbon fibre and Li and deepens the understanding of the design parameters for tailoring multifunctional carbon fibres used in improved structural batteries.

Keywords: multifunctional composites, energy storage, carbon fibres, lithium insertion, microstructure, heteroatoms, atom probe tomography, synchrotron hard X-ray photoelectron spectroscopy, Auger electron spectroscopy

Preface

The work in this thesis was carried out from June 2019 to August 2023 at the Division of Materials and Manufacturing, Department of Industrial and Materials Science, Chalmers University of Technology. The research was financially supported by Energimyndigheten under project number 46598-1.

Acknowledgements

To properly convey my gratitude towards Professor Fang Liu, my main supervisor, would surely require more words than can fit in this entire thesis. Yet, I want to try to express at least a fraction of all that appreciation. Over these four years, Fang has been unwavering in her dedication to my research and to my development as a scientist. Such commitment from such a brilliant person might be the greatest gift one can receive. Thank you, Fang, for your countless hours and infinite enthusiasm. You have made something as tough as PhD studies feel so joyful and fantastic. I also want to extend a heartfelt appreciation to Professor Leif Asp, my co-supervisor, who I met more than eight years ago, and who has ever since been an integral part of my path and education. Thank you, Leif, for all the innumerable opportunities, big and small, that you have provided, and which have propelled my journey to something truly enjoyable.

Moreover, I wish to deeply thank Dr Johanna Xu for all our collaborations, all the battery cells you built for me, and all the wonderful discussions we have had. And thank you Dr Eric Tam, for your vital help with everything concerning electron spectroscopy. Dr David Carlstedt, Dr Shanghong Duan, Carl Larsson, and Ruben Tavano, I want to thank you all for our work together. It has been a privilege to be a part of the excellent structural battery team at Chalmers. Learning and simultaneously having fun – is there any better multifunctionality?

I also want to thank the structural battery team at KTH Royal Institute of Technology, and especially Professor Dan Zenkert, for always being welcoming and generous in sharing knowledge and insights. Furthermore, I'm grateful to Dr Mahander Singh and Professor Baptiste Gault for inviting me to Max-Planck-Institut für Eisenforschung and helping me with the final and crucial atom probe work.

And of course, I must shout out a big thank you to all my colleagues and friends at Chalmers for lovely times both at and outside work. I have had so much fun with you! Special thanks goes to my office mate and confidante, Rasmus Gunnerek, for all hilarious moments.

Finally, I want to thank my family and friends. You being there and lifting me up has kept me going during this long and winding trek, and as I now reach the finish line, I hope to embrace you all.

Thesis

This thesis consists of a summary of the research performed and the following appended papers:

- Paper I** **Best practices for analysis of carbon fibres by atom probe tomography**
M. Johansen, F. Liu
Microscopy and microanalysis, Vol 28, p 1092–1101, 2022.
<https://doi.org/10.1017/S1431927621012812>
- Paper II** **Mapping nitrogen heteroatoms in carbon fibres using atom probe tomography and photoelectron spectroscopy**
M. Johansen, C. Schlueter, P.L. Tam, L.E. Asp, F. Liu
Carbon, Vol. 179, p 20–27, 2021.
<https://doi.org/10.1016/j.carbon.2021.03.061>
- Paper III** **Lithiated carbon fibres for structural batteries characterised with Auger electron spectroscopy**
M. Johansen, J. Xu, P.L. Tam, L.E. Asp, F. Liu
Applied Surface Science, Vol. 627, 157323, 2023.
<https://doi.org/10.1016/j.apsusc.2023.157323>
- Paper IV** **Suppressing lithium migration in carbon fiber negative electrode during atom probe tomography analysis**
M. Johansen, M.P. Singh, B. Gault, F. Liu
Manuscript
- Paper V** **Unravelling lithium in electrochemically active carbon fibres with atom probe tomography**
M. Johansen, M.P. Singh, J. Xu, L.E. Asp, B. Gault, F. Liu
Manuscript

Contribution to the appended papers:

Paper I: Fang Liu suggested the approach. Marcus Johansen executed the experimental work and analysis of the results. Marcus Johansen and Fang Liu wrote the paper.

Paper II: Fang Liu suggested the approach. Marcus Johansen executed the atom probe tomography experiment and analysis. Pui Lam Tam executed the X-ray photoelectron spectroscopy experiments, Christoph Schlueter executed the hard X-ray photoelectron spectroscopy experiments, and Marcus Johansen analysed the data. Marcus Johansen and Fang Liu wrote the paper. Leif Asp, Pui Lam Tam, and Christoph Schlueter proof-read the paper and contributed with suggestions and comments.

Paper III: Marcus Johansen suggested the approach. Johanna Xu assembled and cycled the electrochemical cells. Marcus Johansen executed the Auger electron spectroscopy experiments. Pui Lam Tam executed the X-ray photoelectron spectroscopy experiments. Marcus Johansen analysed the data. Marcus Johansen and Fang Liu wrote the paper. Johanna Xu, Pui Lam Tam, and Leif Asp proof-read the paper and contributed with suggestions and comments.

Paper IV: Marcus Johansen and Fang Liu suggested the approach. Johanna Xu assembled and cycled the electrochemical cells. Marcus Johansen and Mahander Singh performed the experimental work. Marcus Johansen analysed the data. Marcus Johansen and Fang Liu wrote the paper.

Paper V: Marcus Johansen and Fang Liu suggested the approach. Johanna Xu assembled and cycled the electrochemical cells. Marcus Johansen and Mahander Singh performed the experimental work. Marcus Johansen analysed the data. Marcus Johansen and Fang Liu wrote the paper. Mahander Singh, Johanna Xu, Leif Asp, and Baptiste Gault proof-read the paper and contributed with suggestions and comments.

Papers not included in the thesis:

J. Xu, W. Johannisson, M. Johansen, F. Liu, D. Zenkert, G. Lindbergh, L.E. Asp, “Characterization of the adhesive properties between structural battery electrolytes and carbon fibres”, *Composite Science and Technology*, Vol. 188, 2020, 107962, <https://doi.org/10.1016/j.compscitech.2019.107962>

L.E. Asp, K. Bouton, D. Carlstedt, S. Duan, R. Harnden, W. Johannisson, M. Johansen, M.K.G. Johansson, G. Lindbergh, F. Liu, K. Peuvot, L.M. Schneider, J. Xu, D. Zenkert, “A structural battery and its multifunctional performance”, *Advanced Energy & Sustainability Research*, 2021, p 2000093, <https://doi.org/10.1002/aesr.202000093>

J. Xu, Z. Xia, J.S. Sanchez, M. Johansen, F. Liu, L.E. Asp, “Coating of LFP/graphene oxide on carbon fibres as positive electrodes for structural batteries”, Proceedings of the 20th European Conference on Composite Materials: Composites Meet Sustainability, Lausanne, Switzerland, 2022

S. Duan, F. Lindelöw, Z. Li, Z. Ma, Y. Li, J. Xu, D. Carlstedt, M. Johansen, L.E. Asp, “Building and characterization of symmetric structural battery”, Proceedings of the 20th European Conference on Composite Materials: Composites Meet Sustainability, Lausanne, Switzerland, 2022

M. Johansen, J. Xu, P.L. Tam, L.E. Asp, F. Liu, ”Effect of lithium insertion on mechanical properties of individual commercial PAN carbon fibres for multifunctional composites”, Proceedings of the 20th European Conference on Composite Materials: Composites Meet Sustainability, Lausanne, Switzerland, 2022

J. Xu, Z. Geng, M. Johansen, D. Carlstedt, S. Duan, T. Thiringer, F. Liu, L.E. Asp, “A multicell structural battery composite laminate”, *EcoMat*, 2022, e12180, 2022. <https://doi.org/10.1002/eom2.12180>

J. Xu, C. Creighton, M. Johansen, F. Liu, S. Duan, D. Carlstedt, P. Mota-Santiago, P. Lynch, L.E. Asp, “Effect of tension during stabilization on carbon fiber multifunctionality for structural battery composites”, *Carbon*, Vol 209, 2023, 117982, 2023. <https://doi.org/10.1016/j.carbon.2023.03.057>

M.S. Siraj, S. Tasneem, D. Carlstedt, S. Duan, M. Johansen, C. Larsson, J. Xu, F. Liu, F. Edgren, L.E. Asp, “Advancing Structural Battery Composites: Robust Manufacturing for Enhanced and Consistent Multifunctional Performance”, *Advanced Energy & Sustainability Research*, 2023, 2300109, <https://doi.org/10.1002/aesr.202300109>

Contents

ABSTRACT	I
PREFACE	III
ACKNOWLEDGEMENTS	III
THESIS	V
CONTENTS	IX
LIST OF ABBREVIATIONS	XI
1 INTRODUCTION	1
1.1 MOTIVATION.....	1
1.2 AIM AND OBJECTIVES	3
1.3 SCOPE.....	3
2 BACKGROUND	5
2.1 LITHIUM-ION BATTERIES	5
2.2 CARBON FIBRE COMPOSITES.....	8
2.3 STRUCTURAL BATTERIES.....	9
2.4 CARBON FIBRES	11
2.4.1 <i>Manufacturing</i>	11
2.4.2 <i>Microstructure</i>	12
2.4.3 <i>Properties</i>	14
3 EXPERIMENTAL METHOD	17
3.1 MATERIALS.....	17
3.2 APT.....	20
3.3 FIB/SEM.....	23
3.4 XPS AND HAXPES.....	25
3.5 AES.....	28
4 RESULTS & DISCUSSION	31
4.1 UNCYCLED CARBON FIBRES.....	31
4.1.1 <i>Developing APT methodology</i>	31
4.1.2 <i>Revealing the atomic makeup</i>	38
4.2 LITHIATED CARBON FIBRES	40
4.2.1 <i>Developing AES methodology</i>	41
4.2.2 <i>Micro-scale mapping of Li: individual fibres</i>	43
4.2.3 <i>Expanding APT methodology</i>	46
4.2.4 <i>Nano-scale mapping of Li: individual atoms</i>	47
5 SUMMARY OF APPENDED PAPERS	53
6 OUTLOOK	55
REFERENCES	57
APPENDED PAPERS	67
PAPER I.....	71
PAPER II.....	83
PAPER III.....	93
PAPER IV	103
PAPER V.....	119

List of Abbreviations

AES	Auger electron spectroscopy
APT	atom probe tomography
EELS	electron energy loss spectroscopy
FIB	focused ion beam
HAXPES	hard X-ray photoelectron spectroscopy
HM	high modulus
IM	intermediate modulus
PAN	polyacrylonitrile
SEI	solid-electrolyte interphase
SEM	scanning electron microscopy
TEM	transmission electron microscopy
XPS	X-ray photoelectron spectroscopy

1 Introduction

The idea that energy storage can be “massless” is a provocative one. Especially so in an age of electric vehicles hampered by limited driving range. However, such an idea is possibly made true by a concept called *structural batteries*. Imagine an electric vehicle free of heavy battery packs but propelled by energy stored in its frames and panels. In these structural batteries, one of the pivotal constituents are carbon fibres, which can host lithium in their microstructure. For the field of structural batteries, a fundamental understanding of carbon fibres’ microstructure, chemical information, and interaction with lithium is needed. As a response, this thesis aims to provide just that.

1.1 Motivation

The consumption of fossil fuels has been one of the primary drivers of economic growth and development since the industrial revolution but must now be reduced due to mainly two reasons. (i) Combustion of fossil fuels releases greenhouse gases that trap heat from the sun, leading to global warming and climate change. The consequences of climate change are devastating to humankind as it creates more frequent extreme weather events and erodes life’s support structures in the form of ecosystems [1]. (ii) The finite nature of fossil fuels means that their availability will eventually diminish, leading to price increases and supply shortages. This poses a threat to energy security, economic stability, and global development.

Ending our dependence on fossil fuels is therefore crucial, and we can do that through using renewable energy sources. However, this transition is challenging. Not least in the transport sector, where the internal combustion engine vehicle has reigned supreme for decades. The electric vehicle has been described as the successor, but multiple hurdles remain before it can completely dethrone the internal combustion engine vehicle [2]. The greatest shortcoming of the electric vehicle is possibly the relatively limited energy storing capacity of conventional lithium-ion batteries, which makes the electric vehicle inferior when it comes to driving range.

Increasing the driving range of electric vehicles might seem trivial as one could simply just use more batteries, however, there are practical limitations concerning size and weight. More batteries will add significant weight to the vehicle, reducing its efficiency and performance, and take up more space, limiting the passenger and cargo capacity. Therefore,

the solution falls on increased energy density. There are many different routes to this end, where the most obvious, though far from trivial, ways tend to look at energy density on the battery level. Another, less apparent, way is to view the problem through the holistic lens of the whole vehicle. How can the energy density of the whole vehicle be increased? The answer is multifunctional devices [3], [4] that integrate electrochemical energy-storage into structural systems. This effectively eliminates the weight of energy storage. Such multifunctional devices are called structural batteries [5]–[7], and can be claimed to provide “massless” energy storage.

The structural battery combines the functions and components of carbon fibre composites and lithium-ion batteries (Figure 1.1). The integration of these two fields hinges on the use of the different properties of carbonaceous materials. In conventional lithium-ion batteries, graphite is commonly used as the negative electrode material, while high-performance lightweight composites rely on carbon fibres as the reinforcement material. However, in the structural batteries, carbon fibres serve a dual purpose, acting both as reinforcement and negative electrode. Consequently, the carbon fibre must fulfil not only its traditional mechanical load-bearing role but also store electrochemical energy by hosting lithium ions in its microstructure.

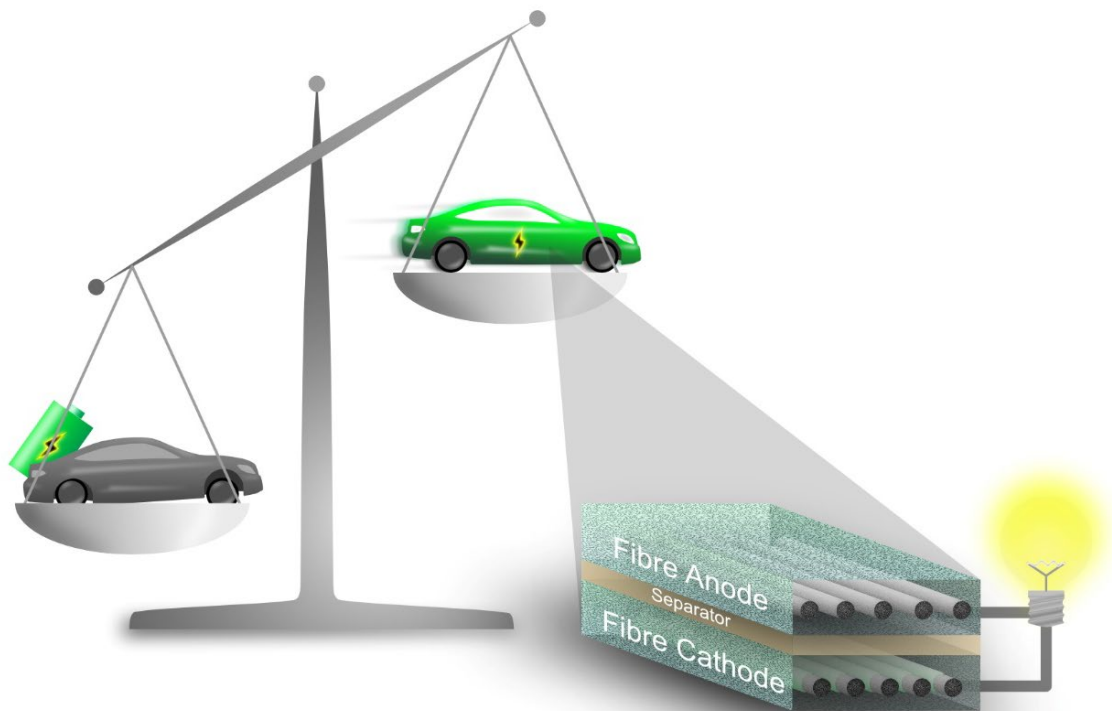


Figure 1.1: Conceptual schematic of a structural battery, and the mass reduction it offers when implemented in an electric vehicle.

To enhance the structural battery, it is essential to understand the relationship between the microstructure of the carbon fibre and its mechanical and electrochemical properties. While several studies have been conducted on this topic, there is still a significant knowledge gap regarding the configuration and distribution of elements within carbon fibres, especially carbon fibres exposed to electrochemical cycling. This knowledge is critical for gaining a comprehensive understanding of the multifunctionality of the carbon fibres and developing them effectively. Therefore, this thesis uses advanced material characterisation techniques to reveal information about the atoms in electrochemically uncycled and cycled carbon fibres.

1.2 Aim and objectives

The aim of this research is to advance the fundamental understanding of the atomic make-up of carbon fibres, and to elucidate carbon fibres interactions with lithium. To achieve this aim, the research can be broken down into the following objectives:

- Develop the methodology of performing APT on uncycled carbon fibres. This methodology is described in **Paper I**.
- Determine the distribution and chemical configuration of atoms in uncycled carbon fibres. This is presented in **Paper II**.
- Develop the methodology of performing APT on cycled carbon fibres. These methodologies are described in **Paper IV** and **Paper V**.
- Determine the distribution and chemical configuration of lithium in cycled carbon fibres. This is presented in **Paper III** and **Paper V**.

1.3 Scope

This work investigates commercial PAN-based carbon fibres for structural batteries with mass spectrometry and electron spectroscopy techniques to understand the fibres' microstructure.

2 Background

For a long time, the fields of lithium-ion (Li-ion) batteries and carbon fibre composites were separate disciplines. However, that changed in the beginning of the 2000s, when the two fields produced an offspring in the form of structural batteries that can store electrochemical energy *and* carry mechanical load simultaneously. This new field still strives to balance the vastly different personalities inherited from its parent fields, but the crucial link holding them together is the multifunctionality of carbon fibres. Here follows an overview of Li-ion batteries, carbon fibre composites, structural batteries, and the process-microstructure-property relationship of carbon fibres.

2.1 Lithium-ion batteries

The Li-ion battery possesses high gravimetric and volumetric energy density, which makes it ideal to power mass and size-sensitive electric devices such as portable electronics and electric vehicles [8]–[11]. Through reversible redox reactions the Li-ion battery is rechargeable as it can convert electrical energy into chemical energy, and vice versa. The battery design (Figure 2.1) typically consists of an anode of carbon-based material and a cathode of Li-containing transition metal oxide or phosphate [12], [13]. The electrodes are placed in an ion-conducting electrolyte on either side of a separator. During charging, the electrical bias applied in an external circuit forces electrons and Li^+ to leave the cathode to the anode via separate paths. The electrons travel in the external circuit while the ions move through the electrolyte and the separator. As the ions arrive at the anode, they each gain one electron [14]. Since energy was required for the transfer, the ion is now found in a less energetically favourable state relative the initial state and has gained an electrochemical potential relative the cathode. The more ions that have been transferred; the more energy is stored. Thus, the capacity of the anode to host Li partly determines the capacity of the battery. When the applied electrical bias is ceased, the ions will migrate back to the more energetically favourable state in the cathode, and the electron flow is reversed. If the external circuit leads through an electric device, the current of electrons will power the device.

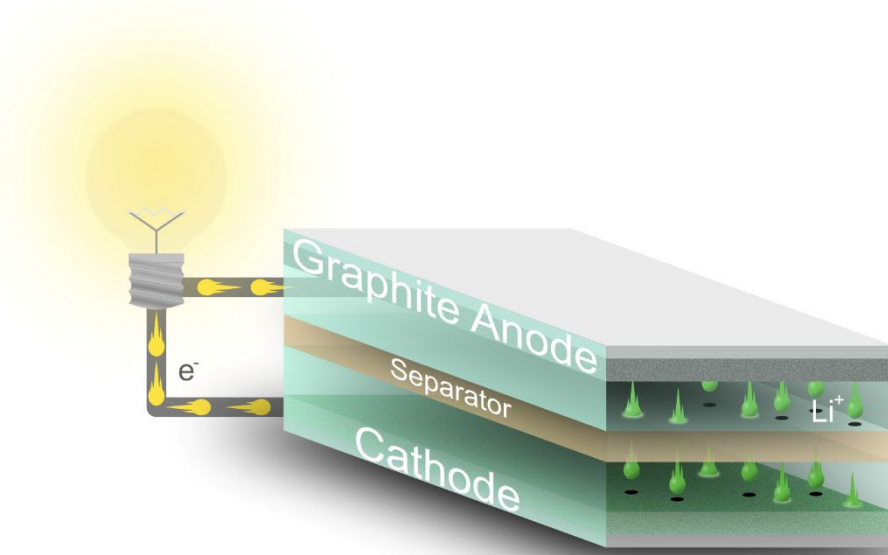


Figure 2.1: Schematic of a lithium-ion battery during discharge. Electrons move from the anode via the external circuit to power an electric light bulb and then on to the cathode, while Li ions leave the anode via the electrolyte, through the separator, and enter the cathode.

The anode must provide a material structure able to accept and release Li for many cycles without degrading [13]. Graphite, which is the most common anode material, consists of stacked graphene layers that can be viewed as storage shelves for Li to be placed on [15]–[17]. The structure of the individual layers are hexagon networks of sp^2 -hybridized carbon (C) atoms. Most graphene layers in pure graphite have a Bernal stacking sequence (ABA order) where the parallel layers are shifted relative each other, so that half the C atoms locate above another C atom, and the other half above the centre of a hexagon hole (Figure 2.2a). The intercalation of Li dilates the interplanar spacing and skews the stacking sequence to a hexagonal one (AAA order, or rather AIAIA with I being the layer of intercalated ions). Here, every C atom hover over another C atom (Figure 2.2b), while Li position between the hexagons of adjacent graphene layers [16], [18]. However, the in-plane neighbouring hexagons remain unoccupied due to atomic repulsion to other Li [17]. Thus, one Li can be accommodated for every six C – a stoichiometry expressed as LiC_6 . From the electrochemical perspective this means that for every six C at most one electron can be exchanged. With the number of exchanged electrons, z , Farady’s constant, F , and the molar mass, M , of six C atoms, the theoretical specific capacity of graphite, Q , can be calculated to 372 mAh/g:

$$Q = \frac{zF}{M}. \quad (\text{Equation 2.1})$$

However, due to defects and disorder, a more realistic stoichiometry is expressed as Li_xC_6 ($x < 1$). For example, a disordered stacking sequence, also known as turbostratic structure (Figure 2.2c), can impede intercalation and diminish capacity [19]. If the carbon material is allowed to become even more disordered and reach the opposite end of the scale to graphite, it is called “hard carbon”. In hard carbon the graphene layers do not stack and are instead nonparallel (Figure 2.2d). Without the confines of held together layers, Li is allowed to bond on both side of the graphene layers [20], giving a stoichiometry of Li_2C_6 with twice as much Li and twice the theoretical capacity – 744 mAh/g [19]. However, the combined factors of hard carbon’s lower volumetric energy density, slanting discharge profile, and lower initial Coulombic efficiency have made it less attractive than graphite as anode material for Li ion batteries [13]. But not only the right type of disorder, but also the right type of defects can lead to improved capacity. Carbon materials doped with “impurities” like nitrogen (N) heteroatoms has proved to yield enhanced electrochemical capacity [21]. For example, graphene and mesocarbon microbeads have improved reversible capacity after N-doping [22], [23].

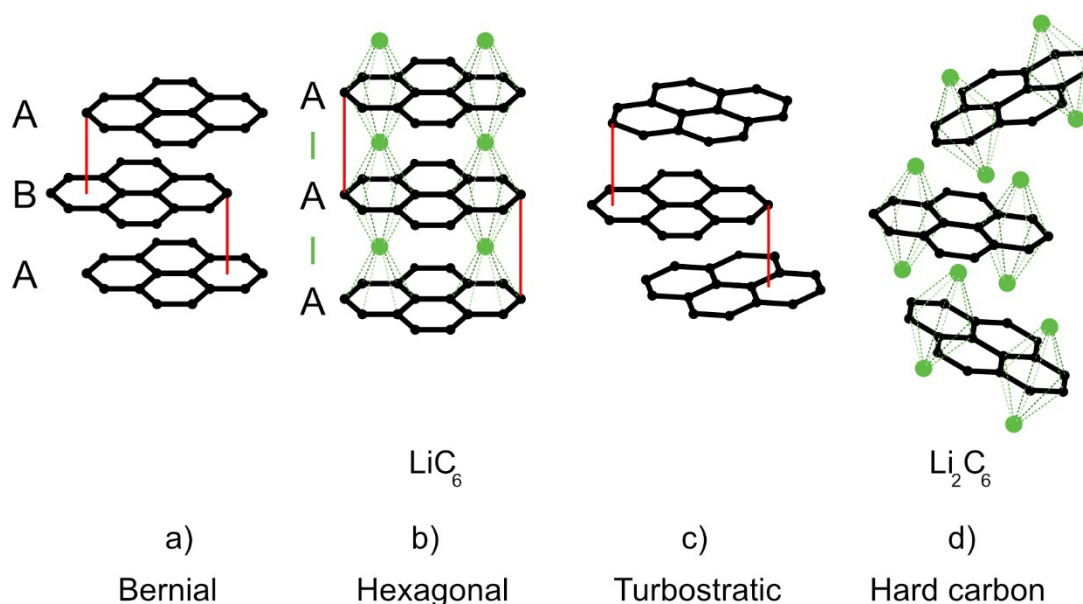


Figure 2.2: a) Graphitic carbon with ABA stacking, b) graphitic carbon with AAA stacking after Li insertion, c) turbostratic carbon, and d) disordered hard carbon.

The boundary between the electrodes and the electrolyte is also very important for the electrochemical performance [12], [13], [24], [25] as it is the entry point of the Li ions being shuttled back and forth between the electrodes. Ideally, reduction and oxidation only take place at the electrodes and the electrolyte remain unaffected by the electric potential. However, electrolytes do not withstand an infinitely large range of potentials and may break down when exposed to too high or low voltages [12]. This is problematic as a large potential difference between the electrodes is desirable [16]. Often the stability window of an electrolyte encompasses the high potential at the cathode, whereas the low potential of the graphite anode falls below the electrolyte’s reduction potential. Consequently, the

electrolyte will decompose in contact with the graphite. Fortunately, with the right type of electrolyte, instead of a continuous break down, a passivation layer is created on the surface of the anode – a so called solid-electrolyte interphase (SEI) – that shields the electrolyte and the anode from each other. This layer is a complex product of the electrolyte's components (solvents, salts, and additives), which is reflected in the composition of mixed organic and inorganic compounds. A proper SEI prevents further electrolyte reactions from occurring but is still ionically conductive and allows Li ions to pass between electrolyte and anode. The SEI is, however, not an infallible and static barrier, but may degrade or change in morphology due to repeated electrochemical cycling and other external conditions [26], which will induce more electrolyte reactions and trap more inactive Li [24], [27]. Therefore, the integrity of the SEI is of great importance.

The deposition of metallic Li on the graphite anode, so-called Li plating, is another important, yet undesired, aspect of the reactions at the surface of the anode [28]. To begin with, this leads to capacity fade through deactivation of Li, but continuous plating may evolve into safety hazardous growth of Li dendrites that eventually pierce the separator and short-circuits the battery cell. Li plating occurs when the supply of Li at the anode surface outpaces the ability of the anode to accommodate Li. In general, this happens through overcharging an already fully charged anode or owing to overpotentials from fast charging and low operation temperatures. However, in actuality, Li plating is a very complex phenomenon, and has also been encountered in battery cells experiencing mild conditions [29].

Even though the text above is primarily concerned with the anode, it is evident that Li-ion batteries are delicate devices consisting of many components working together in harmony. It can thus be appreciated that it presents an interesting challenge to complicate the situation further by requiring the battery to also carry mechanical load.

2.2 Carbon fibre composites

A composite material combines two or more materials into a single entity with greater performance than its parts. In structural applications, a discontinuous phase (reinforcement) is embedded in a continuous phase (matrix). The matrix protects and fixes the mechanically superior reinforcement in a favourable arrangement to transfer external loads in a desired way [30]. In composite materials with continuous fibrous reinforcement, the composite's properties and behaviour are dictated by the orientation of the fibre – stiffer and stronger in the direction of the fibre. Thus, the properties can be tailored. Typically, fibre composites are laminated structures consisting of layers of unidirectional fibres. As a result, fibre composites are generally anisotropic. However, depending on the desired properties, the layers can be stacked with different orientations relative to each other (Figure 2.3).

In lightweight applications, carbon, glass, or aramid fibres are commonly used with a matrix of thermosetting or thermoplastic polymer. Carbon fibre reinforced polymer composites offer an excellent specific modulus and specific strength, approximately

55 MNm/kg and 240 kNm/kg, respectively, compared to aluminium 2024-T4 with approximately 27 MNm/kg and 150 kNm/kg [30]. Due to their superior properties, carbon fibre composites are ideal for lightweight applications in aerospace, automotive, naval, storage tank, and wind turbine industries, as well as for sports equipment such as sports cars, fishing rods, tennis rackets, and golf clubs.

Carbon fibre composites offer not only a lightweight structural solution, but from a multifunctionality standpoint also present the potential for various functions. The multi-component system of carbon fibre composites lends itself to merge with other multi-component systems such as Li-ion batteries.

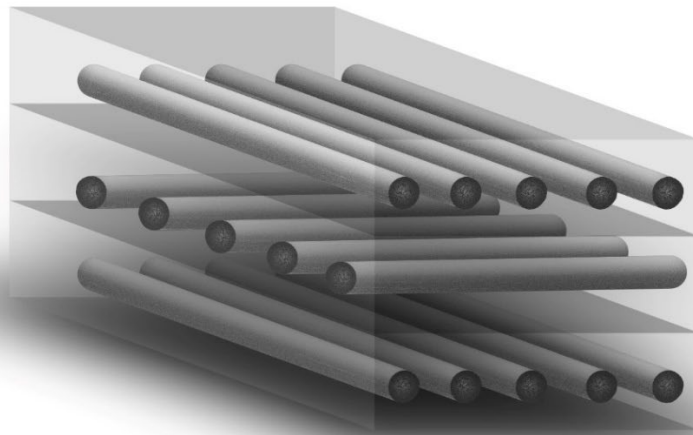


Figure 2.3: Fibre composite laminate with upper and lower layers in the 0° direction, and the middle layer in the 90° direction.

2.3 Structural batteries

The structural battery is a fusion of the Li-ion battery and the structural composite into a multifunctional device able to store electrochemical energy and carry mechanical loads [5], [31], [32]. Various architecture concept exists, but they all rely on carbon fibres to act as reinforcement and anode material, while a matrix material transfers mechanical load and transports Li ions. Generally, the architectures of structural batteries can be divided into laminated and three-dimensional. The laminated is the most common architecture, which consists of a carbon fibre tow as anode stacked on top of a separator and a cathode material (Figure 2.4). The cathode is either conventional with the active material adhered to a metal foil current collector, or novel with active material coated on a carbon fibre tow acting as current collector and reinforcement [33], [34]. The stack is impregnated by a structural battery electrolyte, that after curing separates into a bi-continuous system of a porous polymer network permeated by a liquid electrolyte [35], [36]. With the three-dimensional architecture, each carbon fibre is coated with a structural electrolyte separating the fibre

from the matrix, which is filled with cathode particles. Thus, each coated fibre is an individual battery cell.

In the early 2000s, the initiative research on structural batteries was conducted at Army Research Laboratory in USA [37]–[40], where researchers aspired to make a laminated structural battery with carbon fibres as negative electrode, a metal mesh with LiFePO_4 as positive electrode, and a glass fibre weave as separator [38]. The mechanical performance was promising, but the electrochemical performance was underwhelming owing to poor electrical insulation. Liu *et al.* endeavoured in 2009 to build a structural battery with a gel electrolyte, which yielded acceptable electrochemical properties, but inadequate mechanical properties [41]. Over the coming years, substantial progress was made towards building a truly multifunctional structural battery with high mechanical and electrochemical performance [31], [42]. Asp *et al.* demonstrated in 2021 a structural battery boasting unparalleled multifunctionality with tensile strength passed 300 MPa, elastic modulus of 25 GPa, and energy density at 24 Wh/kg, [6]. Shortly after, in 2022, Xu *et al.* presented the first multicell structural battery [43], and in 2023 Siraj *et al.* improved the robustness of the manufacturing process [44].

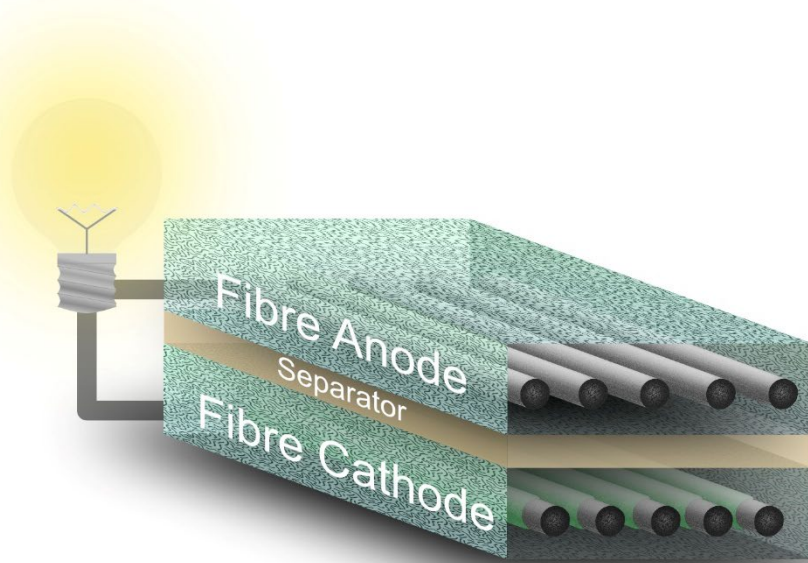


Figure 2.4: Schematic representation of a structural battery with laminated architecture.

Over the two decades, most components and concepts of structural batteries have seen reformulations. However, a constant from the very start has been the carbon fibre. For a long time, carbon fibres were only designed for optimal mechanical performance. Many different types of commercially available fibres have been tested and characterised [45], [46], but it was not until 2023 that the first carbon fibres tailored for the purpose of multifunctionality were presented [47]. As ultimately even the carbon fibre sees redesign, it becomes important to understand them in-depth.

2.4 Carbon fibres

Carbon fibres act as reinforcement in lightweight composite materials in a wide range of industries: automotive, aerospace, naval, sporting goods, storage tanks, and wind turbines. The demand for carbon fibres is predicted to be 400 000 tonnes by 2035 [48], [49]. The process of manufacturing carbon fibres is a delicate operation, that the industry companies understandably are reluctant to share, and as a result the public knowledge regarding the relationship between process and properties of the carbon fibres is limited [50]. Typically carbon fibre have a diameter of 5-7 μm and consists of at least 92 wt% C [51], with the other elements being N and oxygen (O). Carbon fibres are conventionally used as structural reinforcement owing to their exceptional specific strength and stiffness, but in recent years, the ability of the carbon fibre to simultaneously work as a battery electrode, has led to deepened research on carbon fibres [31]. The properties of a carbon fibre are governed by the microstructure, which in turn is governed by the manufacturing.

2.4.1 Manufacturing

For a fundamental understanding of the carbon fibre, it is appropriate to begin with its precursor. Ideally the precursor cost-effectively converts into a carbon fibre with high carbon content. Rayon, polyacrylonitrile (PAN), pitch, and lignin are examples of precursors. In the beginning, carbon fibres were made from rayon, but the lower production cost of PAN and pitch quickly became more desirable [52]. Pitch-based carbon fibres have ultra-high modulus but are brittle, while PAN-based carbon fibres balances stiffness and strength. The main part of today's carbon fibres are PAN-based, though the production is energy intensive and depend on finite resources [53]. Therefore, the interest in plant-based lignin carbon fibres is increasing. Nevertheless, this thesis focuses solely on PAN-based carbon fibres since they are the most suitable fibre type for structural battery composites [54].

Acrylonitrile converts into carbon fibres in several steps: polymerisation, spinning, thermal stabilisation, carbonisation, and graphitisation. The acrylonitrile monomers are during polymerisation joined into PAN chains. Processability is improved by adding 2-15% of comonomers. The PAN chains are aligned and stretched into fibres during spinning [50], [52], [53], [55], [56]. The length and alignment of the chains affect the properties of the fibre. After fibre spinning the carbon content is 50-60% and the diameter $\sim 15 \mu\text{m}$ [50], [55].

High temperature is required to merge the chains into stiff and strong graphene layers, but the PAN chains are thermally instable. Therefore, they are first stabilised via oxidation at 200-300°C, where they passes through an oxidising atmosphere with zones of increasing temperature, and the chains cyclises into thermally stable ladder structures [52], [53] (Figure 2.6a). At this stage, the fibre consists of 62–70 wt% C, 20–24 wt% N, 5–10 wt% O, and 2–4 wt% hydrogen (H) [53].

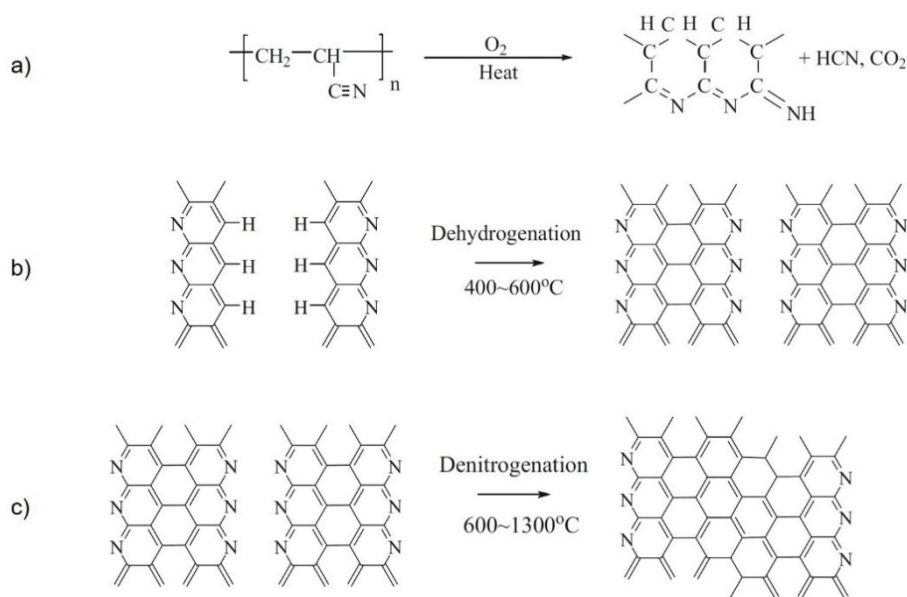


Figure 2.6: Illustration of the heat treatment steps for oxidation and carbonisation of carbon fibres. a) Cyclisation of PAN through oxidation into heteroatomic ladder structures. b) Cross-linking through dehydrogenation into ribbon structures. c) Fusion through denitrogenation into graphene-like sheets. Adapted from Ref. [50] with permission from Springer Nature.

After stabilisation, the fibre can withstand the higher temperatures required for carbonisation (up to 1600°C) and graphitisation (up to 3000°C). Further oxidation is avoided with inert atmosphere, which often is nitrogen gas. The carbonisation expels much of the non-carbon atoms and shrinks the fibre diameter to $\sim 5\text{--}7\text{ }\mu\text{m}$ [50], [56]. In the first heating zone at 400–600°C, dehydrogenation and elimination of hydroxyl groups cross-link the ladder structures into wider ribbon structures bound by nitrogen (Figure 2.6b). In the second heating zone at 600–1600°C, denitrogenation cross-links the ribbon structures into graphene-like sheet structures in small crystallites (Figure 2.6c). However, some non-carbons still remain: N and O. If carbon fibres with small crystallites and high strength is desired, carbonisation may be the final heat treatment. On the other hand, if large crystallites, high conductivity, and high modulus is sought, graphitisation is conducted up to about 3000°C. At such elevated temperatures, nitrogen gas reacts with the carbon fibre, and instead argon is used. With graphitisation further non-carbons are expelled, the crystallites grow, and the alignment of the crystallites is increased [52]. Surface treatment is the final manufacturing step. The fibres are coated with sizing, a thin polymer layer protects the fibre from surface damage, eases handling, and increases compatibility with the matrix.

2.4.2 Microstructure

The heterogenous microstructure of carbon fibres consists of crystalline and amorphous domains with ubiquitous nano-pores. The crystallites formed during carbonisation are turbostratically stacked graphene layers (Figure 2.2c), that are rather aligned in the longitudinal direction of the fibre [50], [52]. The layers are held together by weak bonds of

van der Waals forces, while the in-plane sp^2 -hybridised graphene bonds constitutes one of the strongest bonds in nature (~ 5.9 eV) [57]. Thus, the structure and properties of the crystallites are anisotropic.

Historically, most investigations of the microstructure of carbon fibres have focused on crystallography, and the analysis techniques have been many. Among them are X-ray diffraction [58]–[63], Raman spectroscopy [62], [64], and transmission electron microscopy (TEM) [58], [63]–[69]. These techniques are typically used to characterise the crystallites and amorphous domains in carbon fibres and relate them to mechanical properties. The size of the crystallites is described by the longitudinal length L_a and the thickness of the graphene stack L_c (Figure 2.7). The interlayer distance in the crystallites, d_{002} , is a measure of the degree of graphitisation. A value approaching the interlayer distance of pure graphite of 3.35 Å indicates a higher degree of graphitisation.

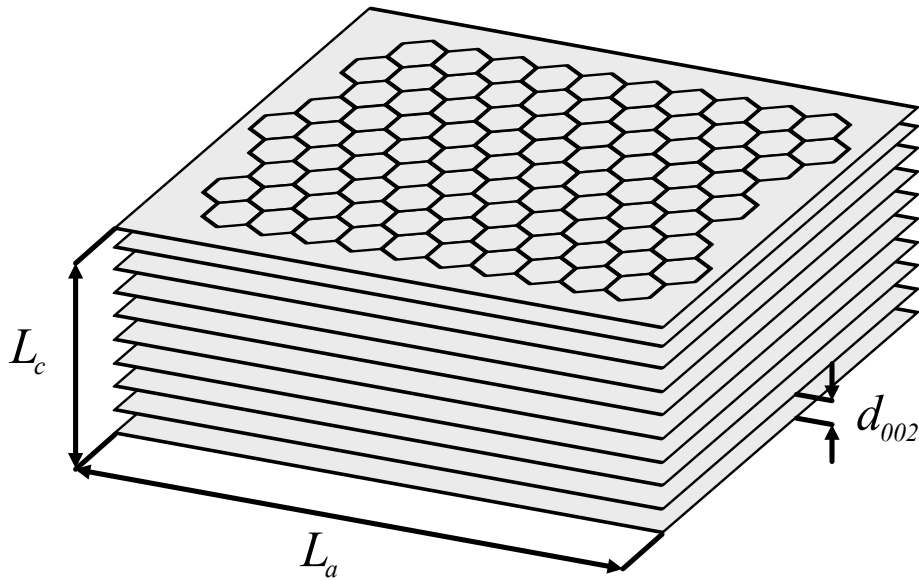


Figure 2.7: Schematic illustration of a crystallite of stacked graphene layers. L_c is the crystallite thickness, L_a is the longitudinal length, and d_{002} is the interplanar distance.

Techniques instead used to determine the chemical character of carbon fibres are X-ray photoelectron spectroscopy (XPS) [52], [70] and electron energy loss spectroscopy (EELS) coupled to TEM [67], [68]. The major elements detected are C, O, and N. XPS has mostly been used to investigate the surface and adhesion properties of carbon fibres to increase compatibility with matrix materials in composites [52]. Conventional XPS can distinguish chemical states of atoms, but struggles with elements of low concentrations, such as the relatively low levels of N in carbon fibres. To clearly reveal chemical state of all elements in carbon fibres, we use synchrotron hard X-ray photoelectron spectroscopy (HAXPES) in this thesis (Section 3.4).

Angle resolved XPS has also been used to examine the atomic composition across the cross-section of carbon fibres, albeit with poor resolution [70]. High in-plane spatial resolution on carbon fibres has been achieved with EELS [67], [68]. However, the transmission projection of EELS only yields spatial information in two dimensions, as it compresses three-dimensional information in the thickness direction. In this thesis, the atomic distribution is uncovered in three dimensions with atom probe tomography (Section 3.2).

2.4.3 Properties

The size and orientation of the crystallites affect the mechanical properties of a carbon fibre. Larger crystallites and greater alignment generate higher axial tensile modulus [59]. However, owing to the anisotropy of the microstructure, the transverse modulus of carbon fibres can be up to 30 times lower than the axial modulus [71]. Although graphene boasts to be one of the strongest materials, a carbon fibre has a tensile strength many times lower due to the flaws in the microstructure. Since large crystallites experience higher risk of inducing critical flaws, carbon fibres with smaller crystallites usually have higher tensile strength [56], [59].

Carbon fibres can be categorised based on their tensile modulus into two types: intermediate modulus (IM) fibres with modulus <300 GPa and high modulus (HM) fibres with a modulus >300 GPa. IM fibres carbonised up to 1600°C as final heat treatment, and thus have relatively small crystallites and high tensile strength (strength-to-modulus ratio greater than 1%). HM fibres, on the other hand, are graphitised up to 3000°C , which makes them grow larger crystallites, but the tensile strength is reduced (strength-to-modulus ratio smaller than 1%) [50], [64]. Crystallite size and orientation also affect thermal and electrical conductivity. The larger and more aligned crystallites of HM fibres result in higher conductivity than IM fibres [72]. Additionally, the anisotropic microstructure of carbon fibres leads to poor interplanar conductivity, but enables very high intraplanar conductivity in the graphene layers [73], [74].

Lithium can be hosted in the microstructure of carbon fibres, and thus carbon fibres can act as battery electrodes [31]. HM fibres with higher degree of graphitisation are easy to expect to have higher capacity than IM fibres, however, in reality the opposite is true. HM fibres only reach a electrochemical capacity ~ 150 mAh/g, while IM fibres reach ~ 350 mAh/g [46], [75]. As explained in Section 2.1, two carbon structures can host Li ions: either in the ordered crystalline structure, or the disordered amorphous structure. The carbon fibre consists of both types of structure. However, in the carbon fibre the ordered domain is not graphitic, but turbostratic, which obstructs the Li ions to properly intercalate between the graphene layers. The obstruction is more severe in the HM fibre with its big crystallites, and consequently the IM fibre performs better by hosting more lithium in the amorphous domain [64].

Lithiation affects the properties of the carbon fibre. To be able to accommodate Li, the carbon fibre expands both in the axial and radial direction: $\sim 0.7\%$ and $\sim 6.6\%$, respectively [76]. As Li is expelled during delithiation, the carbon fibre contracts, but some volume change is irreversible, which likely is due to trapped Li in the microstructure [77]. The tensile strength is also affected, as it is reduced by lithiation and partly restored by delithiation. Stiffness, nonetheless, is constant during lithiation [78], and capacity is unaffected by tensile strain [79].

Today's PAN-based carbon fibres are fortunately electrochemically active, even though they were not designed with such capabilities in mind. This means that there are great potentials for improvement. Commercially available T800 carbon fibres consist of ~ 96 at% carbon (C), ~ 3 at% nitrogen (N), and ~ 1 at% oxygen (O) [80], which means that the average stoichiometry of a hexagon can be represented as $C_{5.76}N_{0.18}O_{0.06}$. If it is assumed that each hexagon either binds one Li like in graphite ($LiC_{5.76}N_{0.18}O_{0.06}$), or two Li like in hard carbon ($Li_2C_{5.76}N_{0.18}O_{0.06}$), then the theoretical maximum capacity in an assumed perfectly crystalline T800 ranges from 368.8 mAh/g to 737.6 mAh/g. Measured capacity of T800 after ten cycles with charge rate of 0.1C is 243 mAh/g [46]. Consequently, it can be said that only $\sim 33\%$ to $\sim 66\%$ of the available carbon atoms are effectively used to bind Li. Based on the measured capacity the stoichiometry of a fully lithiated T800 is estimated to $LiC_{8.8}N_{0.25}O_{0.06}$, which corresponds to ~ 10 at% Li. However, this is a lower boundary as any contribution from trapped Li has been neglected. Thus, actual measurement of the Li concentration and distribution in lithiated carbon fibres is needed to understand what microstructure limitations must be overcome in contemporary carbon fibres in order to design new multifunctional carbon fibres for structural batteries.

3 Experimental Method

Over the course of this work, carbon fibres in electrochemically uncycled and cycled states were investigated with mass spectrometry and electron spectroscopy techniques. The first section of this chapter presents the investigated polyacrylonitrile (PAN) based carbon fibres; how these fibres were assembled into electrochemical cells; and how these cells were electrochemically cycled. This is followed by descriptions of the techniques used to investigate the carbon fibres at different length scales. The imaging mass spectrometric technique of atom probe tomography (APT) was used to create three-dimensional reconstructions of the atom distribution on the nanometre scale. The tiny samples required for APT were prepared with combined focused ion beam and scanning electron microscope (FIB/SEM). To study the chemical configuration and distribution of the elements on the micrometre scale, electron spectroscopy techniques were used: X-ray photoelectron spectroscopy (XPS), synchrotron-based hard X-ray photoelectron spectroscopy (HAXPES), and Auger electron spectroscopy (AES).

3.1 Materials

Many types of commercially available carbon fibres can act as negative electrode in structural batteries [45], [75]. Our investigation focuses on three types of commercial PAN-based carbon fibres: M60J, T800, and IMS65. Of the three fibre types, M60J is manufactured with a higher final heat treatment temperature that generates larger crystallites (Figure 3.1a), which yield higher stiffness, higher thermal conductivity, and lower electrical resistivity. M60J is categorised as a high modulus (HM) fibre. T800 and IMS65 are intermediate modulus (IM) fibres. Their smaller crystallites (Figure 3.1b-c) give rise to higher tensile strength and higher electrochemical specific capacity. The physical and electrochemical properties of the fibres are summarised in Table 3.1. We singled out these fibre types since their physical properties and crystallite sizes were known from previous studies [46], [64], [75]. Furthermore, they represent three tiers of specific electrochemical capacity: 154 mAh/g (M60J), 243 mAh/g (T800), and 317 mAh/g (IMS65).

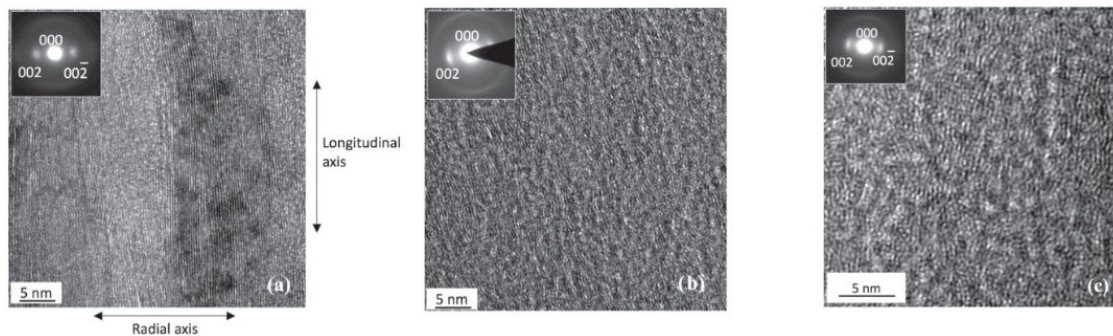


Figure 3.1: TEM micrographs of the microstructure of carbon fibres. a) The more ordered microstructure of M60J. b) The less ordered microstructure of T800 and c) IMS65. Adapted from Ref. [64] with permission from IOP Publishing.

Table 3.1: Physical properties, crystal structure and electrochemical performance of M60J, T800, and IMS65. Reproduced from Ref. [80]. CC BY 4.0.

	M60J	T800	IMS65
Final heat treatment temperature range (°C)	1800-3000	1100-1600	1100-1600
Tensile modulus (GPa)	588	294	290
Tensile strength (MPa)	3920	5490	6000
Electrical resistivity ($\Omega \cdot \text{cm} \times 10^{-3}$)	0.7	1.4	1.45
Thermal conductivity ($\text{cal}/(\text{cm} \cdot \text{s} \cdot \text{K})$)	0.363	0.0839	-
Average crystal length (\AA)	>300	18	19
Average crystal thickness (\AA)	>100	18	28
Interlayer spacing (002) (\AA)	3.47	3.70	3.49
1 st cycle capacity (mAh/g)	159	265	358
10 th cycle capacity (mAh/g)	154	243	317

In the study on uncycled carbon fibres' chemical composition, all three fibre types were investigated. Nevertheless, as the work progressed to lithiated carbon fibres, the focus was narrowed to just T800. This was motivated by much of the concurrent research on structural batteries opting for T800 as negative electrode material [6], [81]. This choice might seem baffling as IMS65 is on par with T800 in terms of mechanical properties and has better specific capacity. However, such high capacity as 317 mAh/g is only seen for unsized IMS65, but with the sized IMS65 the capacity drops to 212 mAh/g [46]. Without sizing, the fibres become difficult to handle during cell assembly and the fibres' adhesion to the matrix material is weakened. Sized T800, on the other hand, has optimal properties, including a capacity of 243 mAh/g.

Electrochemical half-cells with lithium metal as counter electrode were built (Figure 3.2). The fibres were supplied by Oxeon AB as tows spread to unidirectional ultra-thin tapes with a linear weight of 0.52 g/m (TeXtreme®, T800SC-12k-50C), and attached with conductive silver paint to a copper current collector. The tow thickness was $\sim 25 \mu\text{m}$, corresponding to five layers of fibres. The separator was a glass microfiber filter (Whatman GF/A, 260 μm thick). The cells were sealed in pouch bags with laminated constructions of PET/Al/PE from Skultuna Flexible with layer thicknesses of 12 μm , 9 μm , and 75 μm ,

respectively. A tow of T800, a Whatman separator, and a sheet of lithium metal were stacked and soaked in an electrolyte consisting of 1.0 M LiPF_6 in ethylene carbonate and diethyl carbonate 50:50 wt%.

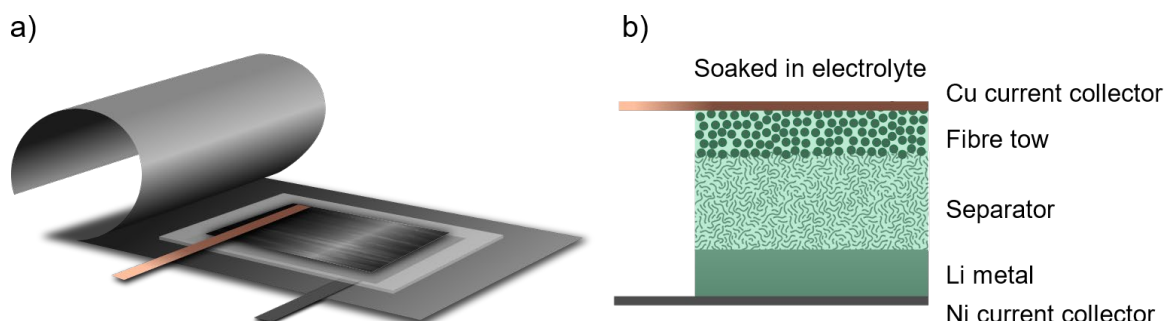


Figure 3.2: Electrochemical half-cell. Schematic of a) a carbon fibre-lithium metal cell in an opened pouch bag, and b) its cross-section.

The cells were assembled in a glove box with dry argon atmosphere (<1 ppm H_2O , <1 ppm O_2), and charge/discharge cycled with a battery cycler from Neware (CT-4008-5V10mA-164). The potential window was 1.5 V and 0.01 V versus Li/Li^+ , considered to correspond to delithiated and lithiated carbon fibres, respectively. All cells underwent four galvanostatic cycles with low currents corresponding to 0.1C based on the theoretic maximum capacity of graphite of 372 mAh/g. The final cycles, however, differed, and they are summarised in Table 3.2. After cycling, the cells were disassembled inside the inert atmosphere of the glove box, where the fibre tows were dried overnight. Finally, the fibres were transferred to the instruments in a transfer vessel to prevent them from exposure to ambient air. Lithiated carbon fibre that are unprotected over long periods show extensive formation of oxides (Figure 3.3).

Table 3.2: Final cycle condition for electrochemical cells.

Cell name	C-rate final cycle	Final state of lithiation	Number of cycles
Cell 1	0.05	100 %	5
Cell 2	0.05	50 %	5
Cell 3	0.05	0 %	5
Cell 4	0.2	0 %	5

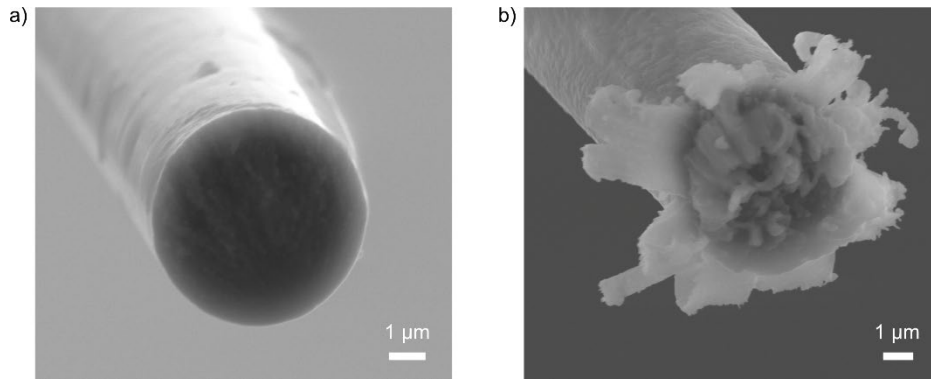


Figure 3.3: SEM micrographs of a) an uncycled carbon fibre, and b) a lithiated carbon fibre, which has oxides formed on the surface after very short exposure to ambient air. Reproduced from Ref. [82].

3.2 APT

APT is a destructive characterisation technique that can visualise the relative position of individual atoms in a tiny material volume [83]. Simply put, the analysed material volume is deconstructed one atom at the time, the atom's initial position and elemental character is deduced, and the material volume is digitally reconstructed (Figure 3.4).

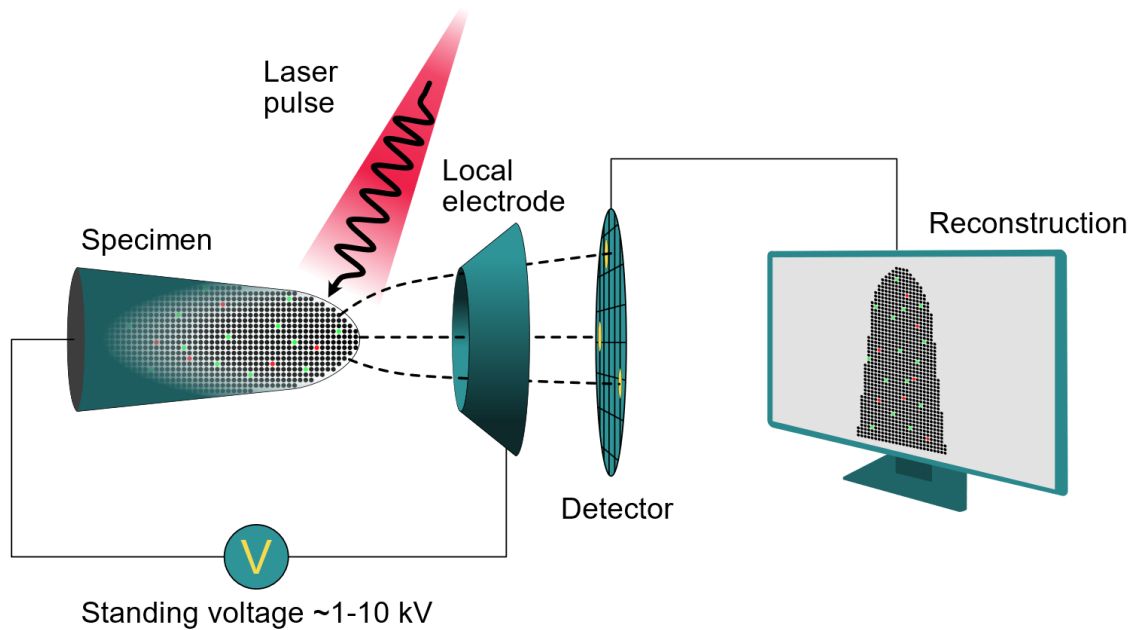


Figure 3.4: Schematic representation of a laser-pulsed local electrode atom probe.

Working principle

The key physical phenomenon of APT analysis is field evaporation, i.e., removal of surface atoms by a high electric field. The field is created by an imposed potential difference between the cryogenically cooled specimen (≤ 100 K) and a close-proximity local electrode. The strength of the electric field builds towards the critical limit for field evaporation,

typically 10-100 V/nm. The smaller the surface area gets, the larger the electric field gets. Therefore, APT specimens are needle-shaped with small tip radii of around 50 nm and the applied voltage around 1-10 kV. When the field is sufficiently strong, the probability is high that the local bond holding the atom to the specimen surface is broken, and the atom is ionised and emitted as a positive ion. The field required for the evaporation is contingent on the element and the surrounding environment. Field evaporation happens selectively at the sharpest edge as that is where the local field is the highest. As the evaporation process continues, the most protruding place on the tip is sequentially shifted to a new atom, and thereby the evaporation sequence can be approximated [83].

Voltage induced evaporation is only effective for materials with electrical conductivity higher than 10^2 S/cm i.e. primarily metals [84]. For less conductive materials, such as carbon fibres, the electric field is combined with thermal activation from a laser. The heating from the laser can shift the required field strength lower (Figure 3.4).

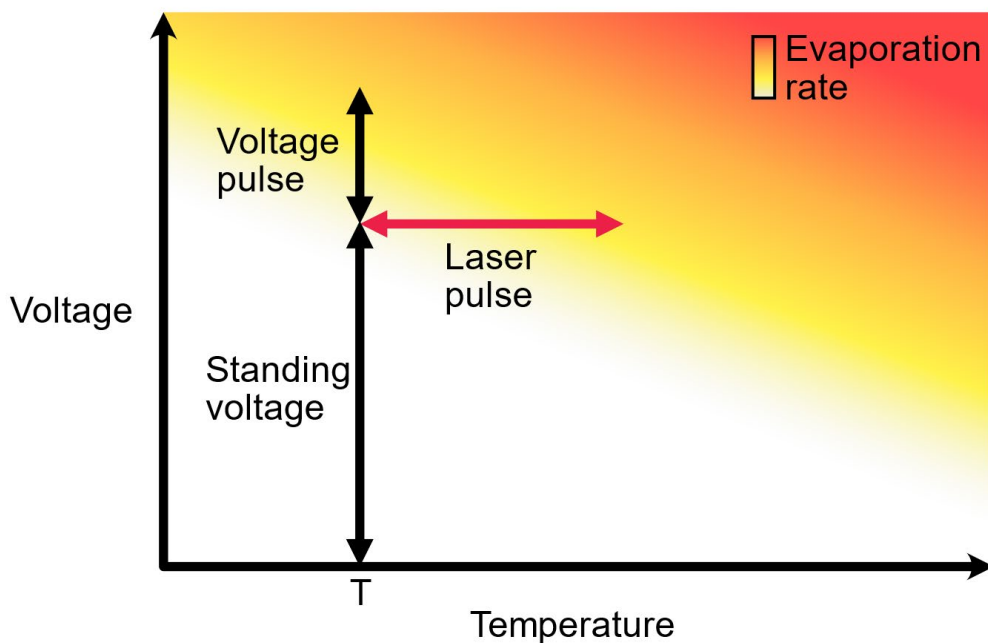


Figure 3.5: Schematic representation of the relation between specimen temperature, voltage, and evaporation rate.

An evaporated ion soon passes through the central circular aperture of the local electrode and thereafter does not experience any field before reaching the detector. The time separating laser pulse and detector hit is recorded and defined as the time-of-flight. With calculation based on the measured time-of-flight, knowledge of distance-of-flight, and applied voltage, the ions can be identified through their mass-to-charge ratio. An ion exposed to an electric field has a potential energy, which is converted into kinetic energy when the atom is ionised and emitted. The potential energy is described as $E_{potential} = neV$, where n is the number of electrons removed from the atom (the charge state of the ion), e the elementary charge, and V the applied voltage. The kinetic energy is described

as $E_{kinetic} = mv^2/2$, where m is the mass, and v the velocity of the ion. The velocity is assumed to be constant, and thus $v = d/t$, where d is the distance-of-flight, and t is the time-of-flight. In the combined energy equation, the mass and charge state of the detected ion can be calculated according to,

$$\frac{m}{n} = 2eV \frac{t^2}{d^2}. \quad (\text{Equation 3.1})$$

The mass-to-charge ratio, m/n , is then used to identify the chemical species of the ion. For example, the mass-to-charge ratio of 7 Da can be assumed to be related to a lithium ion consisting of three protons and four neutrons with a charge state of 1+, ${}^7\text{Li}^{1+}$. However, 7 Da can also be related to a nitrogen ion consisting of seven protons and seven neutrons with a charge state of 2+, ${}^{14}\text{N}^{2+}$. Deconvolution of such overlapping mass-to-charge peaks is discussed in detail in Chapter 4.

Besides recording the time-of-flight, the detector also records the positions of each ion hitting in two dimensions, and thus records the hit location in x- and y-coordinates. Based on the hit location and assumptions on the trajectory, the original position of the ions can be approximated. Progressively, atom after atom is removed from the surface, revealing the layer underneath. The hit sequence of ions along the specimen axis (z-coordinate) is recorded during the sequential evaporation of atoms layer after layer. Thus, every ion gets assigned three coordinates. With the combination of two-dimensional hit location and field evaporation sequence the three-dimensional image can be reconstructed. From the collected data on position coordinates and mass-to-charge ratio, a three-dimensional representation of the original atomic distribution in the probed material is finally possible to reconstruct. [83].

Experimental details

In this thesis, three types of local electrode atom probes (LEAPs) were used in laser pulse mode. In the initial study on uncycled carbon fibres, LEAP 3000X HR from Imago Scientific was used. The laser wavelength was 532 nm and laser pulse duration 12 ps. The detection efficiency was 37%. The specimen temperature was set to 100 K. The acquisition rate was set to 2 ions per 1000 pulses (0.2%). The tip radius and shank angle were estimated by measuring SEM images of specimen tips, before generating reconstruction volumes with IVAS 3.4.3. For the investigation of lithiated carbon fibres, LEAP 5000 XS (straight flight path which gives higher detection level) and LEAP 5000 XR (reflectron which gives higher mass resolution) from CAMECA were used. The laser wavelength was 355 nm. The specimen temperature was set 50 K. The acquisition rate was set to 2 ions per 1000 pulses (0.2%).

3.3 FIB/SEM

A dual beam system with scanning electron microscope (SEM) and focused ion beam (FIB) allows for preparation of microscopic specimens through ion etching, material deposition, and a micromanipulation system. The SEM can be regarded as the eye of the sculptor and the FIB as the sculptor's chisel.

Working principle

SEM images are produced by irradiating a material surface with an electron beam in a raster pattern and detect emitted electrons from each point in the pattern. Thus, SEM images are in grayscale, as the brightness of each pixel represents the relative number of electrons that reached the detector for each scan point in the raster. Many types of electrons are emitted after the beam's interaction with the material, but normally for topographic imaging, secondary electrons are the ones used. The resolution of a SEM can be on the nanometre scale.

FIB can sputter away material with nanometre precision by ion bombardment. Fast-moving ions, often gallium ions (Ga^+), are generated in an ion source and accelerated towards the material to be etched, where the ion collides and sputters away material. A FIB/SEM is often also equipped with a micromanipulator and gas injection system. The micromanipulator is commonly in the shape of a needle, which can be translated in three dimensions. The gas injection system is used to deposit material through chemical vapour deposition. With all these capabilities, FIB/SEM can cut out microscopic pieces of material, adhere the pieces to the micromanipulator with deposition from the gas injection system, and lift and adhere the piece onto a sample holder.

Experimental details

The FIB/SEM used was a dual beam FEI Versa 3D workstation. The ion column and the electron column were at 52° angle relative to each other. The ions were generated at a Ga liquid metal source. The gas injection system was used to deposit platinum (Pt). The micromanipulator was an Omniprobe system.

For uncycled fibres, a stereomicroscope and a tweezer were used to isolate individual fibres from a fibre bundle. In the case of cycled fibres, no stereomicroscope was used since the preparation was done inside a glovebox. The single fibre was placed on a small piece of silicon wafer and adhered at two points with either conductive silver glue or copper tape. To accommodate specimen extraction from both the lateral surface and the cross-sectional surface of the carbon fibre, the mounting of the wafer was performed in two ways. The wafer was adhered either horizontally to an aluminium stub for lateral extraction, or vertically with a free fibre end pointing upwards, sticking out from the wafer, for cross-sectional extraction.

A lift-out technique [85] was applied to prepare APT specimens (Figure 3.5). To protect the region of interest in the carbon fibre from Ga implantation during milling, a $\sim 1\ \mu\text{m}$ thick protective layer of Pt was applied through first electron-beam (2.0 kV and 4.0 nA) and then ion-beam (30 kV and 100 pA) induced deposition. The region of interest was

$15 \times 1.5 \mu\text{m}^2$ for the lateral and $5 \times 1.5 \mu\text{m}^2$ for the cross-sectional extraction. The stage was tilted 22° and the ion-beam (30 kV and 3 nA) milled a coarse trench along the Pt layer and slightly longer than the layer, followed by gentler milling (30 kV and 1 nA). The stage was rotated 180° and the milling repeated on the other side of the protective Pt layer. The stage was tilted 52° , so the sample surface was perpendicular to the ion-beam. The wedge of carbon fibre was cut on one end in the transverse direction, leaving the wedge just held at the other end. The stage was then tilted back to 0° . The needle of the Omniprobe was inserted and attached by Pt deposition to the free end of the wedge. A final small trench was milled at the other end of the wedge to free it from the rest of the carbon fibre. The stage was lowered and a coupon with pre-manufactured micro-posts of silicon (CAMECA) was inserted in the FIB/SEM. The end of the wedge of carbon fibre material was placed on a micro-post, adhered with Pt deposition on one side, cut away from the rest. The process was repeated until the wedge had been consumed, yielding material for 2-5 posts for each lift-out. It should be noted that cross-sectional extraction is limited by the fibre diameter, whereas the yield of lateral extraction is higher per lift-out. Then, the stage was rotated 180° , and adhered with Pt on the other side.

The final step was to mill the material piece into a sharp APT specimen. It was done through a series of annular milling. For the initial milling the acceleration voltage was 30 kV, the ion current was 500 pA, the outer diameter of the milling pattern was $3 \mu\text{m}$, and the inner diameter was $2 \mu\text{m}$. Then the ion current and the inner diameter were gradually decreased to 100 pA and $0.15 \mu\text{m}$, and final polishing at acceleration voltage at 2 kV and ion current 27 pA (Table 3.3).

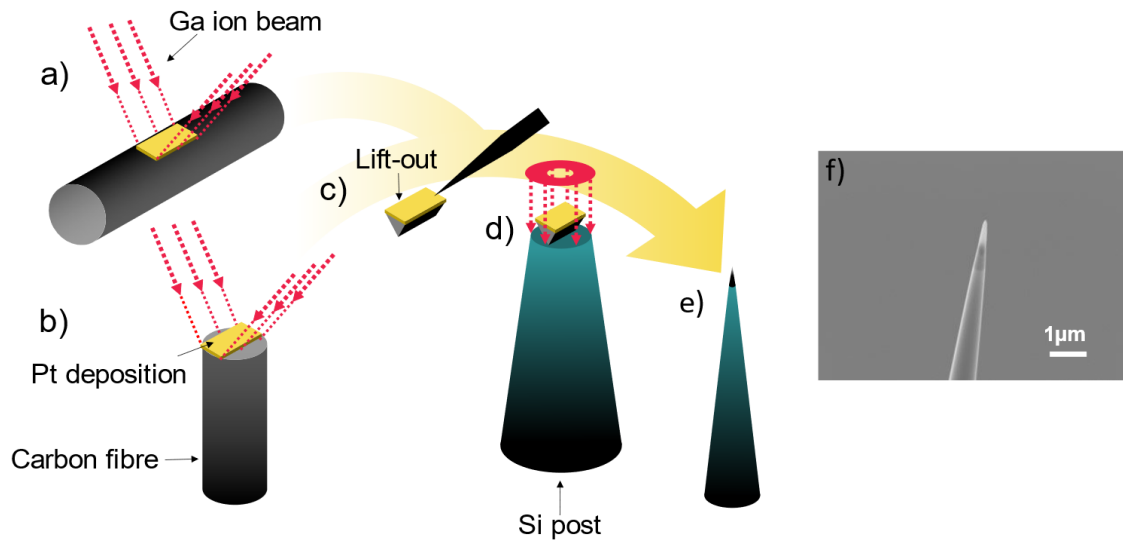


Figure 3.6: Schematic of carbon fibre specimen fabrication for APT. A protective Pt layer is deposited on (a) the lateral or (b) the cross-sectional fibre surface; and the Ga ion beam mills a wedge shape close to the Pt layer. (c) The wedge of carbon fibre is cut free and extracted using the micromanipulator. (d) Part of the wedge is adhered with Pt to a Si post, cut free, and annularly milled to (e) a sharp tip. (f) A SEM image of a sharpened APT tip of carbon fibre. Reproduced from Ref. [80]. CC BY 4.0.

Table 3.3: Instrument settings for FIB milling and polishing for APT specimen preparation.

Inner diameter (μm)	Ion current (pA)	Acceleration voltage (kV)
2.0	500	30
1.5	500	30
1.0	300	30
0.8	300	30
0.5	100	30
0.3	100	30
0.2	100	30
0.15	100	30
0	48	5
0	27	2

3.4 XPS and HAXPES

XPS uses X-rays to irradiate a material sample, which then emits electrons (Figure 3.7). The kinetic energies of these *photoelectrons* are characteristic of the elements present in the material. By measuring the energies, the chemical identity of the material can be revealed. Different types of XPS are categorised based on their X-ray source which can be either a target metal with fixed X-ray energies ~ 1500 eV or a synchrotron with tuneable energies between ~ 2000 and ~ 15000 eV. To distinguish techniques using the elevated energies of “hard” X-rays, the name hard X-ray photoelectron spectroscopy, or HAXPES, is used.

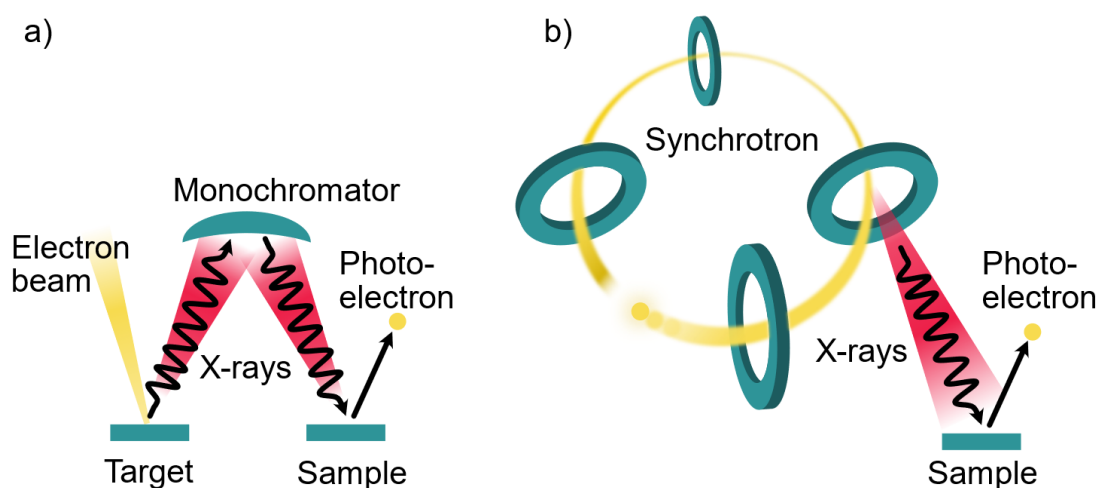


Figure 3.7: Schematic of the principle of a) XPS and b) synchrotron based HAXPES.

Working principle

In XPS, high-energy electrons are bombarded on a target metal which emits X-rays with a continuum background and distinct energy peaks. This energy distribution is narrowed with a monochromator that is setup to only reflect X-rays of a specific wavelength. The selected wavelength is that of the K_{α} radiation for the target metal – often Mg or Al with respective K_{α} radiation energies of 1253.6 eV and 1486.6 eV.

The generated X-rays are projected onto the material to be investigated. The energy of an incident photon, E_{photon} , is absorbed by an electron within the material, and if the absorbed energy is greater than the electron's binding energy to its atomic nucleus, E_{binding} , the residual energy will be converted to a kinetic energy, E_{kinetic} , with which the electron is ejected. The equation of the photoelectric effect, in which ϕ is the work function of the material, can be written:

$$E_{\text{kinetic}} = E_{\text{photon}} - (E_{\text{binding}} + \phi). \quad (\text{Equation 3.2})$$

A photoelectron spectroscope is equipped with a detector that counts electrons and registers their kinetic energy to generate a spectrum. Since the photon's energy is known from the X-ray source, the spectrum of kinetic energies can be translated to binding energies. The binding energy depends on the type of atom and its chemical state. Variations in the local bonding environment of an atom can be detected by subtle peak shifts in the spectrum. For instance, the binding energy of N1s in a nitrogen atom in a graphene layer bonded to *two* carbon atoms (pyridinic-N) is ~ 398.5 eV, whereas in a nitrogen atom bonded to *three* carbon atoms (graphitic-N) is ~ 401.0 eV. However, peaks close to each other can overlap. To determine the fraction of different chemical states the overlapping peaks are deconvoluted with curve fitting software.

X-rays for HAXPES can be generated by a synchrotron light source. A synchrotron is a cyclic particle accelerator that, with strong magnetic fields, can bend the trajectory of electrons traveling at velocities near the speed of light into a closed loop. Electrons forced to change direction emit photons in all directions, i.e., isotropically. However, when changing direction, electrons near the speed of light will experience relativistic effects that make the emission form a cone in the forward direction of the tangent and bumps up the energy of the photons to the X-ray range. This cone of photons has high brilliance, high collimation, high flux, and wide energy tunability range, which gives synchrotron-based HAXPES higher energy resolution and wider range of X-ray energies (~ 2000 - 15000 eV) than conventional XPS with sources of Mg K_{α} (1253.6 eV) or Al K_{α} (1486.6 eV) [86].

Besides higher resolution, the most apparent difference between XPS and HAXPES, is the greater probe depth of HAXPES. Generally, X-rays can travel longer distances than electrons in solids before interacting with matter and losing energy, i.e., the absorption length of X-rays is longer than the inelastic mean free path of electrons. Therefore, deep penetrating X-rays can generate photoelectrons far into the material, but these electrons may not be able to travel the same distance back to the surface of the material without interacting with matter and then reach the detector. Thus, the inelastic mean free path is the limiting factor for the analysis depth. The inelastic mean free path increases with the kinetic energy of the electron, and the kinetic energy depends on the energy of the X-ray. HAXPES utilises much higher X-ray energies, and the consequently higher kinetic energies of the

ejected electrons allow retrieval of deeper situated information. The information depth can be estimated with following expression:

$$\text{information depth} \approx \text{inelastic mean free path} \times \ln\left(\frac{1}{1-(P/100)}\right), \quad (\text{Equation 3.3})$$

where P is the percentage of detected electrons originating within the information depth [87]. In other words, 95% of the detected electrons originate within the depth of approximately three times the inelastic mean free path. With the tuneable X-ray energies of synchrotron HAXPES, different depths can be investigated.

X-ray energies also influence the photoionisation cross-section (the probability of a photon inducing ionisation of an atom and ejecting an electron). The photoionisation cross-section decreases with increased energy of the incident X-ray. Thus, high-energy X-rays yield a less intense spectrum. This has historically prevented the use of hard X-rays in favour of soft X-rays, but with the high brightness of synchrotron light sources, this limitation has been overcome [86].

The photoionisation cross-section is also element dependant, which means that different elements have different probabilities to create photoelectrons, i.e. different elements have different sensitivities. This must be considered for quantitative analysis of intensity spectra. Even though the peak intensities are related to the amounts of elements within the material, the relative peak intensities are skewed due to the difference in sensitivity. Besides photoionisation cross-sections, the peak intensities must also be corrected with instrument specific parameters. The so-called relative sensitivity factors are often used to replace photoionisation cross-sections and instrument specific parameters. Subsequently, the corrected peak intensity can be used to obtain quantitative atomic composition percentage values.

Experimental details

A PHI 5000 VersaProbe III Scanning X-ray Microprobe with a monochromatic $\text{AlK}\alpha$ (fiv = 1486.6 eV) source was used for XPS measurements on uncycled and cycled T800 fibres. During narrow scan for selected elements of interest, pass energy was set to 26.0 eV and the step size to 0.10 eV. Sputter depth profiling was done with an argon (Ar) ion gun with 1 min sputtering intervals. The sputter rate was approximately 145 Å/min, with reference to the tantalum oxide (Ta_2O_5).

HAXPES was performed at the P22 undulator beamline at the synchrotron facility PETRA III (Deutsches Elektronen-Synchrotron, Hamburg) with capabilities of hard X-rays ranging from 2.4 to 15 keV [88]. All three carbon fibre types (M60J, T800, and IMS65) were investigated in their uncycled form. Three X-ray energies were chosen to probe at different depths: 2.5, 4.6, and 7.2 keV. With these energy levels and the inelastic mean free path of graphitic materials approximated according to [89], 95% of the detected photoelectrons were estimated to originate within 17, 28, and 40 nm from the fibre surface for the

respective X-ray energy. The projected beam size for both XPS and HAXPES was around 100 μm . This is much larger than the diameter of a carbon fibre ($\sim 5\text{ }\mu\text{m}$) and means that XPS and HAXPES analyse multiple fibres in one analysis.

3.5 AES

AES uses an electron beam to excite a material to emit Auger electrons. The kinetic energy of the Auger electrons is characteristic to their origin atoms, and thus by measuring that energy, the chemical composition of the material is possible to deduce.

Working principle

In AES an electron beam is focused onto the material to be investigated. When the incident electrons interact with the material, multiple sorts of signals are generated: secondary electrons, backscattered electrons, characteristic X-rays, and Auger electrons (Figure 3.8). The secondary electrons allow for imaging of microstructural features like an SEM, which is an advantage compared to the poor imaging capabilities of XPS. The Auger electrons are generated through a decay mechanism, where an incident electron knocks out an inner-shell electron, creating a vacancy; an electron of higher energy level falls into the vacancy, which releases energy; this energy is transferred to another electron which is then ejected (Figure 3.8). The kinetic energy of the ejected Auger electron thus is the difference between the energy of the transition to fill the vacancy and the binding energy of the ejected electron. Since the energy levels related to the transition and the ionization are dependent on the atom and its surroundings, the measured kinetic energy of the Auger electron can be used to identify the emitting atom and determine its chemical environment.

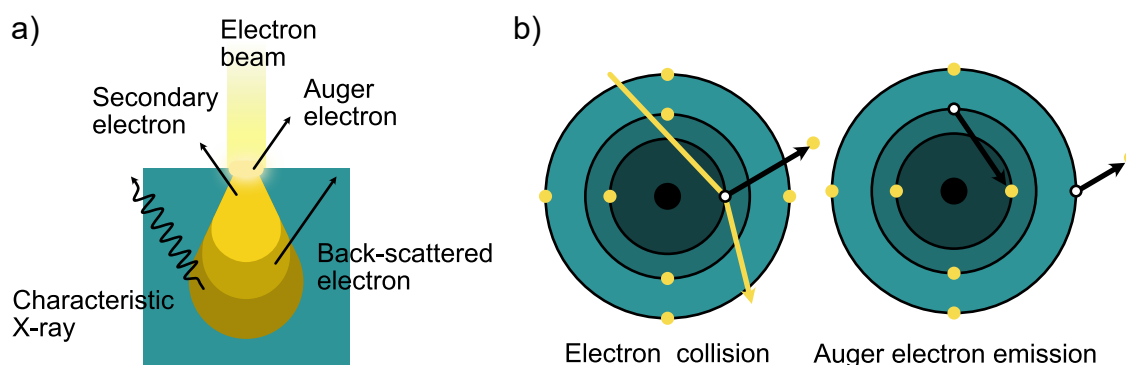


Figure 3.8: The principle of Auger electron emission. a) The incident electron beam interacts with the material and generates different emissions. b) The Auger electrons are generated through the Auger effect.

The kinetic energy of Auger electrons is typically even lower than that of photoelectrons, down to below 100 eV for light elements like Li, giving the Auger electrons a very short IMFP. Thus, only Auger electrons originating close to the surface can avoid being absorbed by the material and then reach the detector. This means that the information retrieved by AES comes from the very top surface atoms, making AES even more surface sensitive than XPS. With the signal from Auger electrons often being weak, the generated spectrum is preferably differentiated to accentuate the signal.

Experimental details

A PHI 700 Scanning Auger Nanoprobe was used for AES experiments. The instrument was equipped with a Schottky field emission electron source, and a cylindrical mirror analyser with energy resolution $< 0.6\%$. The accelerating voltage was set to 3 kV and the beam current to 1 nA. With these settings no beam damage was observed. Survey spectra with a step size of 1.0 eV were scanned from 10 to 700 eV. Depth profiling was performed with an argon (Ar) ion gun with 1 min sputtering at each interval. With reference to the tantalum oxide (Ta_2O_5), the sputter rate was approximately 145 Å/min. To differentiate AES data and smooth the data with Savitzky-Golay filter, MultiPak software (Version 9.7.0.1) was used.

4 Results & Discussion

Our investigation of the atomic construction of carbon fibres simultaneously yielded an array of results useful for the structural battery field and broke new ground for atom probe tomography (APT) and Auger electron spectroscopy (AES). This chapter presents and discusses these results divided into two halves based on the materials analysed: firstly, uncycled carbon fibres; and then electrochemically cycled carbon fibres.

4.1 Uncycled carbon fibres

The first half of this chapter delves into how we used APT together with hard X-ray photoelectron spectroscopy (HAXPES) to reveal the atomic makeup of uncycled carbon fibres. It starts with the development of making APT possible to conduct on uncycled carbon fibres. Then it goes on to understand the effect of N heteroatoms on electrochemical properties of carbon fibres.

4.1.1 Developing APT methodology

Carbon fibres have been a challenging material to analyse with APT, but with the work presented in this thesis we prove that it is possible. A best practice based on experience and experiments follows here for how to reliably conduct APT analysis on carbon fibres with LEAP 3000 X HR. This is told through three aspects that are decisive for the clarity and integrity of the results: acquisition of large data sets; high mass resolution; and accurate interpretation of the data.

Data acquisition

The size of data is most often limited by premature fracture of the specimen tip. To illustrate the high failure rate of APT on carbon fibres, it can be noted that we ran around 40 specimens of uncycled carbon fibre in the LEAP 3000 X HR, but only ten yielded useful results i.e., more than 500,000 ions acquired before fracture. Carbon fibres consist of mainly carbon (C), and small amounts of nitrogen (N) and oxygen (O). Since C requires an exceptionally strong electric field to be field evaporated, carbon fibre specimens in APT is exposed to electric field that induces high mechanical stresses [90] that easily leads to premature specimen fracture. Premature fractures as a cause of too strong electric field can be suppressed by increasing the specimen base temperature and/or the laser energy (Figure 3.5). We found that at 100 K a laser energy of 1 nJ for the 532 nm wavelength laser with pulse duration 12 ps delayed the specimen fracture most efficiently. Furthermore, it proved favourable to avoid the function of *automatic laser scan*. Laser scan is used to ensure intersection of laser beam and tip apex. The laser scan over an area until a position that

generates an adequate evaporation rate is located. If no position is found, the standing voltage is increased before a new scan is conducted. Laser scans were performed for typically every 200 V step until continuous field evaporation is reached. Generally, this happened after 2500 V, but depending on the specimen shape, a blunt tip might not initiate until 5000 V. During acquisition it is usually advised to run automatic laser scan as the apex continuously shifts as an effect of the progressively consumed tip. However, for running carbon fibres with LEAP 3000 X HR we saw that the likelihood of premature fracture increased with the use of automatic laser scan. When laser scanning commenced and the laser moved the continuous evaporation was halted, and afterwards it was nearly impossible for the system without human intervention to resume the same evaporation rate. This led the system to increase the voltage, which eventually resulted in specimen fracture.

The experiments' voltage histories were uneven (Figure 4.1) since sporadic evaporation spikes moved the measured evaporation beyond the set limit, which was followed by the instrument's response to lower the standing voltage until the evaporation fell within the set range. It proved challenging to acquire more than 1 million ions, which was only achieved by four experiment runs. The maximum number of ions acquired during one run was 4.13 million. The sharper specimens ran longer since they required a lower standing voltage to reach a sufficient local electric field. However, their mass resolution was compromised.

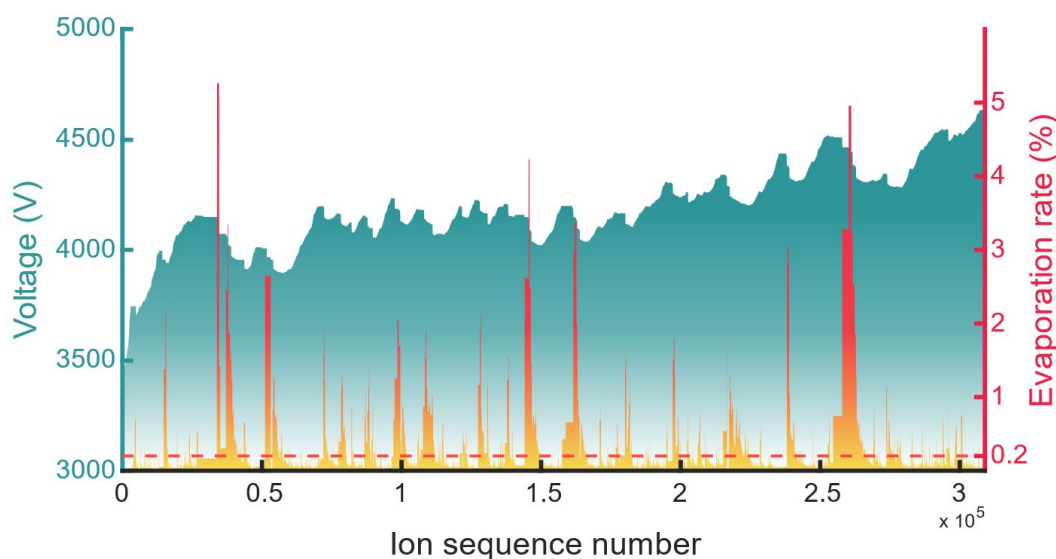


Figure 4.1: Diagram of typical voltage history (left axis) and evaporation rate (right axis) of a carbon fibre run with LEAP 3000 X HR. The dashed line represents the set evaporation rate.

Mass resolution

Proper data interpretation relies on mass-to-charge spectra with narrow and distinct peaks, i.e. high mass resolution. The peak width is dependent on the variation in time-of-flight. For example, if a carbon-12 atom (^{12}C) is ionized to $^{12}\text{C}^+$ and evaporated perfectly timed with the laser pulse it will be registered at 12 Da. But if the evaporation is delayed, the

measured mass-to-charge might come closer to 13 Da and thus get muddled with the satellite peak of carbon-13 atoms (^{13}C). This kind of delayed evaporation is mostly the consequence of residual heat not dissipated from the apex, and it is often manifested in the widened peaks and thermal tails in the mass spectra. Hence, effective heat dissipation is necessary for improved mass resolution. We increased the heat dissipation via three approaches and evaluated their effect on the mass resolving power, $(m/n)/\Delta(m/n)$, with full width at half maximum for the 12 Da peak.

Our first approach was to manufacture blunter tips. The larger cross-section allows more heat to be dissipated. Blunting the tips led to an increase in resolving power from ~ 80 to ~ 570 (Figure 4.2a). Nevertheless, blunt tips require higher voltage to compensate the weaker local electric fields. As explained earlier, high voltage increases the possibility of premature fracture. Therefore, a balance must be found between the mass resolution and the data size. The second approach was to lower the laser pulse frequency. With the laser pulse frequency lowered from 200 to 100 kHz, the mass resolving power increased from ~ 310 to ~ 850 (Figure 4.2b). If the tip is not allowed enough time to cool down between pulses, it risks accumulating heat and generate delayed evaporation. Lower frequency increases the cooling time and the resolution. The third approach was to manufacture the tips so that they aligned the graphene layers in the direction of the heat dissipation. The microstructure and thermal conductivity of carbon fibres are anisotropic due to the alignment of the graphene layers. By extracting the material from the cross-section surface instead of the lateral surface, the mass resolving power was improved from ~ 250 to ~ 580 (Figure 4.2c). However, it should be noted that the lift-out operation from the cross-section is much more difficult and time consuming and yields less material due to the limitations imposed by the size of the diameter. Last, but not least, the material specific behaviour must also be addressed. Due to the different microstructures of HM (M60J) and IM (T800 and IMS65) carbon fibres, they exhibit different thermal conductivity. M60J allowed for much higher mass resolution owing to its greater thermal conductivity (Figure 4.2d).

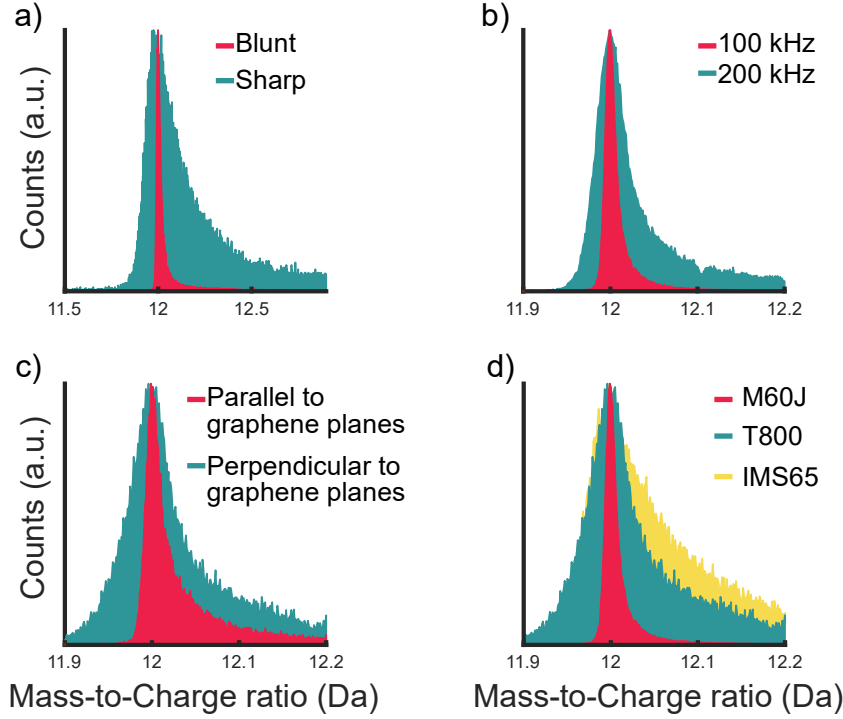


Figure 4.2: Mass resolution comparisons of the peak at 12 Da representing C^+ . The peak width is affected by a) the tip shape, b) the laser pulse frequency, c) the anisotropy of the microstructure, and d) the fibre type.

Data interpretation

Even though carbon fibres consist of at most three elements: C, N, and O, the mass-to-charge spectra are composed of around a hundred peaks (Figure 4.3). Identifying what ion each peak represents is crucial to create a reliable reconstruction. Since M60J contains virtually no N [80] and has higher thermal conductivity, it yields less complex spectra with higher mass resolution. Hence, we first investigated M60J to lay the groundwork for the poorly resolved and more complex spectra of T800 and IMS65.

Carbon is the predominant atom in carbon fibres, and thus it was natural to begin to identify the carbon containing peaks. However, this is not trivial as carbon can field evaporate in molecular ions with x carbon atoms and charge state n : C_x^{n+} . In the experiments, ions ranging in size and charge states from C^+ to C_{22}^{5+} were observed. With 22 ion sizes and 5 charge states, one can imagine 110 types of molecular ions, of which 50 have overlapping peaks in the mass spectra (Table 4.1). Every overlapping peak must be deconvoluted if the analysis should be reliable. Nevertheless, the complexity is increased with the fact that carbon has two stable isotopes: ^{12}C and ^{13}C . On Earth 98.93% of carbon is found as ^{12}C and 1.07% as ^{13}C [91]. With the potential isotopic compositions, the number of possible peaks becomes 1375 of which 885 overlap – a seemingly overwhelming deconvolution challenge. Fortunately, with “small” molecular ions and the low natural abundance of ^{13}C , it is possible to neglect isotope combinations with more than one ^{13}C (Figure 4.4). If only $^{12}C_x^{n+}$ and $^{12}C_{(x-1)}^{13}C^{n+}$ are considered, 220 molecular ions are possible, but the number of

overlapping peaks is only 50, due to the odd number of nucleons in the nucleus of ^{13}C . Non-overlapping coupled with the known natural abundance can be turned into a powerful deconvolution tool. For every peak of $^{12}\text{C}_x^{n+}$ a smaller satellite peak of $^{12}\text{C}_{(x-1)}^{13}\text{C}^{n+}$ is expected with the intensity ratio R being written as

$$R = \frac{x(0.0107 \times 0.9893^{x-1})}{0.9893}. \quad (\text{Equation 4.1})$$

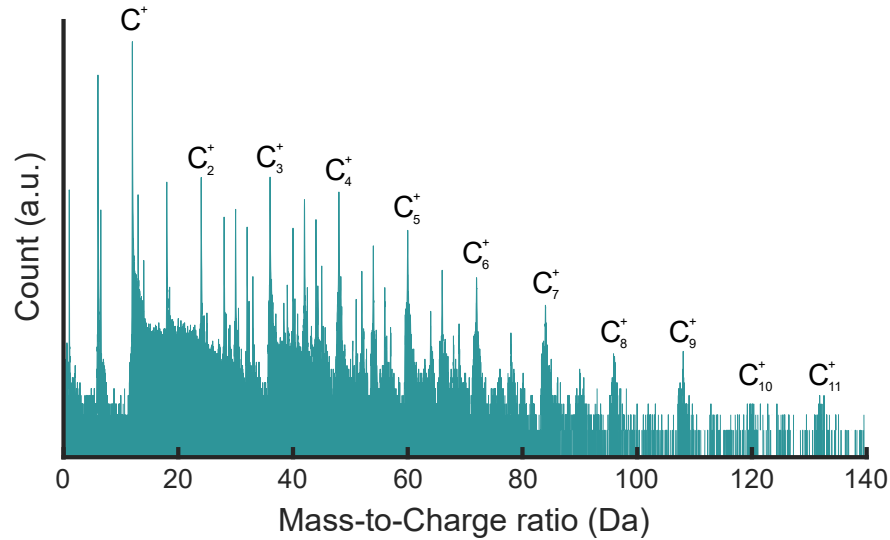


Figure 4.3: Typical mass spectrum of M60J with the C_n^+ peaks marked.

Thus, even though $^{12}\text{C}_3^+$, $^{12}\text{C}_6^{2+}$, $^{12}\text{C}_9^{3+}$, and $^{12}\text{C}_{12}^{4+}$ all have the same mass-to-charge of 36 Da and overlap, the peak can be deconvoluted by using the ratio R together with satellites at 37, 36.5, 36.33, and 36.25 Da (Figure 4.5). It should, however, be noted that this kind of deconvolution completely relies on the ability to distinguish the very small satellite peaks, which is difficult in experiment data with poor quality. This once again underscores the importance of high mass resolution and large numbers of acquired ions.

We used the same deconvolution method to determine overlaps with other ion types. For example, the satellite-to-main peak ratio for C_7^{3+} and C_{11}^{3+} in the measured spectra did not match the theoretical value. This mismatch was attributed to the presence of CO^+ and CO_2^+ which contribute to the peaks at 28 Da and 44 Da, however, without the systematic deconvolution this could have been missed and the oxygen content underestimated.

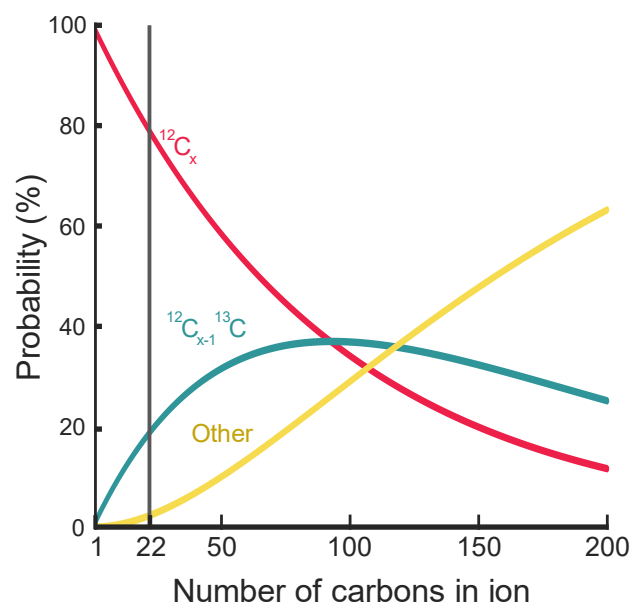


Figure 4.4: Probability of observing different types of molecular ions as a function of the number of carbons based on the natural abundance of carbon isotopes. For small molecular ions (<22 carbon atoms), $^{12}\text{C}_x$ and $^{12}\text{C}_{x-1}^{13}\text{C}$ are significantly more common than other molecular ion combinations.

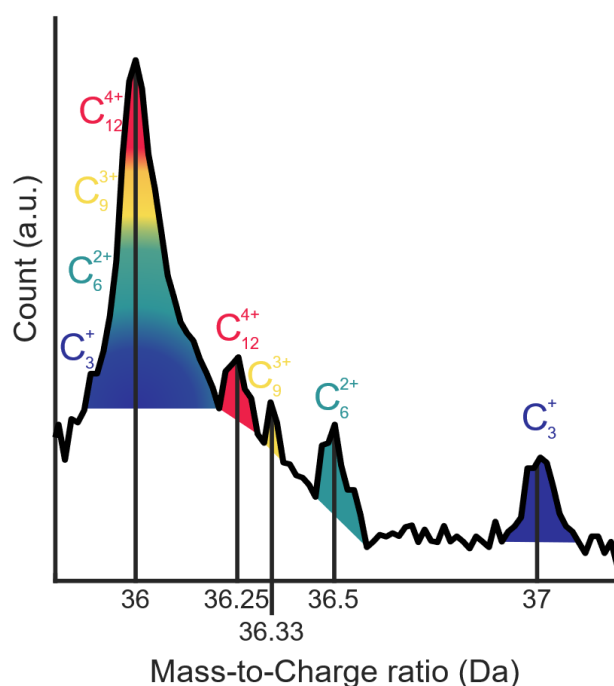


Figure 4.5: The overlapping peaks at 36 Da and their satellite peaks.

Furthermore, the deconvolution method can be used to compensate for count underestimation because of the detector's dead time. Due to the dead time, the detector may fail to register ions that hit with rapid succession within a small area. This phenomenon of course gets more pronounced for ions of the main peaks as their high prevalence makes

them more likely to be involved in a close proximity hit and be affected by the dead time. Subsequently, the main peaks risk to be underestimated, while the satellites show a truer ion count on account of their rarity. Thus the satellites may be used to correct the ion count in the main peaks [92].

Table 4.1: Mass-to-charge for main (M) and satellite (S) peaks of carbon ions and the theoretical ratio between their intensities R . Peaks with blue tiles were encountered in mass spectra of M60J. Reproduced from Ref. [93]. CC BY 4.0.

	Charge state 1+		Charge state 2+		Charge state 3+		Charge state 4+		Charge state 5+		R
	M	S	M	S	M	S	M	S	M	S	
C ₁	12	13	6	6.5	4	4.33	3	3.25	2.4	2.6	1.08%
C ₂	24	25	12	12.5	8	8.33	6	6.25	4.8	5	2.16%
C ₃	36	37	18	18.5	12	12.33	9	9.25	7.2	7.4	3.24%
C ₄	48	49	24	24.5	16	16.33	12	12.25	9.6	9.8	4.33%
C ₅	60	61	30	30.5	20	20.33	15	15.25	12	12.2	5.41%
C ₆	72	73	36	36.5	24	24.33	18	18.25	14.4	14.6	6.49%
C ₇	84	85	42	42.5	28	28.33	21	21.25	16.8	17	7.57%
C ₈	96	97	48	48.5	32	32.33	24	24.25	19.2	19.4	8.65%
C ₉	108	109	54	54.5	36	36.33	27	27.25	21.6	21.8	9.73%
C ₁₀	120	121	60	60.5	40	40.33	30	30.25	24	24.2	10.82%
C ₁₁	132	133	66	66.5	44	44.33	33	33.25	26.4	26.6	11.90%
C ₁₂	144	145	72	72.5	48	48.33	36	36.25	28.8	29	12.98%
C ₁₃	156	157	78	78.5	52	52.33	39	39.25	31.2	31.4	14.06%
C ₁₄	168	169	84	84.5	56	56.33	42	42.25	33.6	33.8	15.14%
C ₁₅	180	181	90	90.5	60	60.33	45	45.25	36	36.2	16.22%
C ₁₆	192	193	96	96.5	64	64.33	48	48.25	38.4	38.6	17.31%
C ₁₇	204	205	102	102.5	68	68.33	51	51.25	40.8	41	18.39%
C ₁₈	216	217	108	108.5	72	72.33	54	54.25	43.2	43.4	19.47%
C ₁₉	228	229	114	114.5	76	76.33	57	57.25	45.6	45.8	20.55%
C ₂₀	240	241	120	120.5	80	80.33	60	60.25	48	48.2	21.63%
C ₂₁	252	253	126	126.5	84	84.33	63	63.25	50.4	50.6	22.71%
C ₂₂	264	265	132	132.5	88	88.33	66	66.25	52.8	53	23.79%

With the spectra of M60J understood, the spectra of N containing T800 and IMS65 were easily interpreted as the same pattern of C and O peaks repeated. The addition of N of course made the spectra more complex by adding, in theory, 26 new peaks assigned as C_xN^{n+} and C_xNO^{n+} (Table 3.5). Furthermore, 5 C_xN^{n+} peaks overlapped with $^{12}C_{(x-1)}^{n+}$, but deconvolution was possible through the use of the main peaks and the expected ratio R . This understanding of how to conduct APT on carbon fibres made it possible for us to really start investigating the microstructure of carbon fibres in a way that had not been done before.

Table 4.2: Mass-to-charge for N related peaks. Peaks with blue tiles were encountered in mass spectra of T800 and IMS65. Reproduced from Ref. [93]. CC BY 4.0.

	Charge state 1+	Charge state 2+	Charge state 3+
N	14	7	4.67
CN	26	13	8.67
C₂N	38	19	12.67
C₃N	50	25	16.67
C₄N	62	31	20.67
C₅N	74	37	24.67
C₆N	86	43	28.67
C₇N	98	49	32.67
C₈N	110	55	36.67
C₉N	122	61	40.67
C₁₀N	134	67	44.67
C₂NO	54	27	18

4.1.2 Revealing the atomic makeup

From previous research it was known that T800 and IMS65 have smaller crystallites and higher capacity than M60J [46], [64]. It was concluded that the smaller crystallites were the reason for the higher capacity for the IM fibres. However, even though, the T800 and IMS65 have similar crystallite size, they differ significantly when it comes to energy capacity. The reason for this was not understood at the start of our work.

Equipped with the knowledge of proper APT conduct for carbon fibres, we created 3D reconstructions of M60J, T800, and IMS65 (Figure 4.6) to help understand how their atomic makeup differ and how this affects their electrochemical capacity. As expected, the atomic concentration of nitrogen heteroatoms in M60J was close to zero. The low N content and large crystallites in M60J are the results of the same high final heat treatment temperature that expels N to graphitise small crystallites into larger ones. These two attributes can affect the capacity, but it is likely that the largest effect comes from the crystallite size. However, neither attribute explains the capacity difference between T800 and IMS65 since they have similar crystallite size, and our APT experiments showed that they have the same average N concentration of ~2.6 at%.

Moving on to analysing the distribution of N heteroatoms in the reconstructions, we expected to find the cause for the capacity difference. In the ideal case N is located at the edges of the graphene planes (Figure 2.6). These edge planes are the entryway for Li, as the basal planes are impermeable. Thus, the more entryways, the easier it is for Li to be inserted into the carbonaceous microstructure, which in the end leads to higher capacity. An even spread of edge planes would hence make the whole microstructure equally accessible, but a carbon fibre possessing agglomerates of N would likely not perform as

well. Nevertheless, the reconstructions of T800 and IMS65 showed equally uniform distributions of N. The mystery of the capacity difference remained.

Even though the distribution of N heteroatoms was uniform, we did not know whether their properties were uniform. Depending on the bonding properties of the heteroatoms, they may have different effects on the carbon networks. APT reconstructions provide information of the elemental character and position of atoms, but the information about atomic bonds is lost. To gain this information, we first employed XPS, however the sensitivity of the instrument was too low to show clear N signals that can be deconvoluted. Synchrotron-based HAXPES, though, proved capable to clearly detect N and variations in peak shape of N1s. The N1s signal was deconvoluted into five peaks (398.5, 399.6, 401.0, 402.2, and 403.8 eV) corresponding to different configurations of N (pyridinic-N, pyrrolic-N, graphitic-N, edge-located graphitic-N, and oxidic-N) (Figure 4.7). Depending on how the N heteroatom configures, the carbon network is disrupted in various ways (Figure 2.4) with differing impact on the electrochemical properties. In general, the N heteroatom either binds to three C atoms, effectively substituting a C atom without breaking the network, or it only binds to two C atoms and thereby severing links in the network. The substitution configuration, Graphitic-N, can lead to a n-type doping and increased electronic conductivity [94] as the N atom has an additional electron to donate to the system. This n-type doping can, however, be nullified by p-type doping generated by configurations of N bonding to only two carbons [95]. The configurations can either belong to a six-membered ring, pyridinic-N, or a five-membered ring, pyrrolic-N. Both sorts create vacancies and edges, that become active sites for Li adsorption, and the capacity of the carbon material is increased [96]–[99]. We compared the amount of pyridinic and pyrrolic-N in T800 and IMS65 and found at last a difference between these two seemingly very similar carbon fibres. IMS65, which has higher capacity (317 mAh/g) than T800 (243 mAh/g), showed to have a larger part pyridinic and pyrrolic-N (20%) compared to T800 (14%). The presence of these disruptive configurations was thus concluded to be the reason for the superior electrochemical capacity of IMS65. The work identified a new design parameter in the form of N heteroatoms, which could be used for future carbon fibre development aimed at structural battery applications.

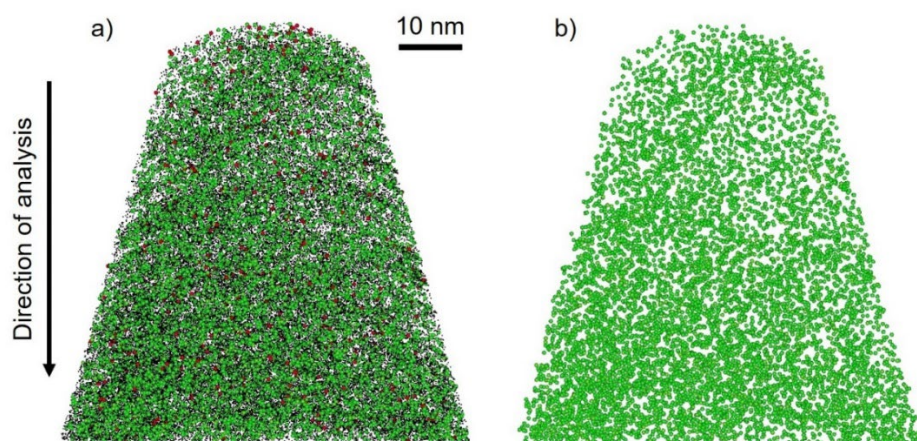


Figure 4.6: 3D reconstructions of an APT tip from T800 with a) all elements showing and b) only N showing. C are represented as black dots, O as red bubbles, and N as green bubbles. For clarities sake, only 5% C, 10% N, and 10% O are shown.

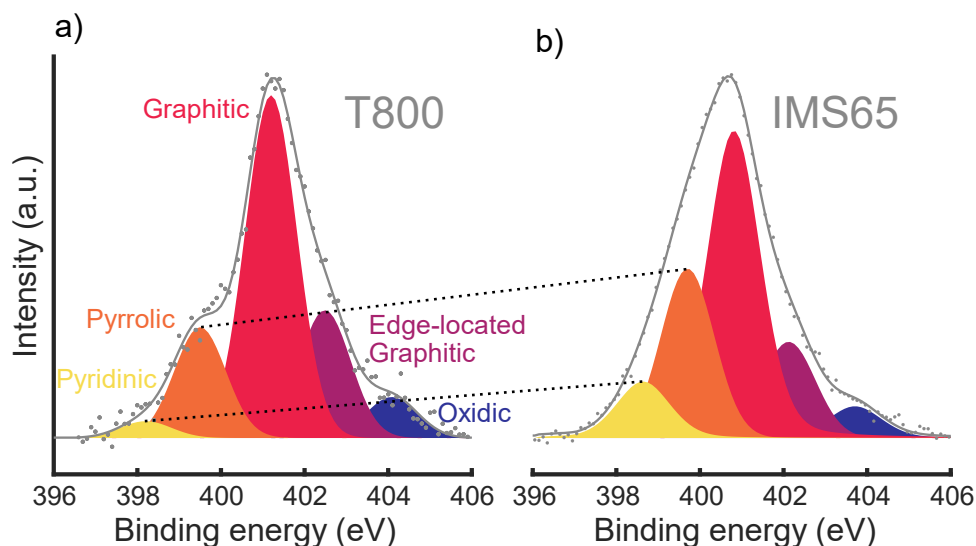


Figure 4.7: Deconvoluted HAXPES peaks of N1s in a) T800 and b) IMS65. Note that the amount of pyridinic and pyrrolic-N is greater in IMS65.

4.2 Lithiated carbon fibres

The second half of this chapter continues into the even more challenging realm of investigating carbon fibres with Li electrochemically inserted into the microstructure. It begins to cover how AES can be used, and how AES spectra can be interpreted to map Li in carbonaceous materials and is followed by the elucidation of how Li is distributed in individual fibres. Then, the efforts of performing APT on lithiated carbon fibres without massive field evaporation of Li is presented, and finally, the atomic distribution of Li in carbon fibres is revealed and its effects explained.

4.2.1 Developing AES methodology

AES generates spectra that are more difficult to quantitatively analyse than XPS spectra, which has held back the popularity of AES. Thus, only sparse studies using AES on battery materials were reported [100]–[107]. This is rather surprising since the technique is well suited for the task. AES is particularly sensitive to Li, one of the lightest elements. We show that AES can distinguish different Li species. Here follows the step we took to harness the capabilities of AES to analyse lithiated carbon fibres.

Our goal was to complement the nano-scale analysis of APT by being able to map the distribution of Li in carbon fibres on the micro-scale encompassing the full transversal cross-section. As a reminder the diameter of a carbon fibre is around 5 μm . Consequently, a technique with spatial resolution high enough to investigate points much smaller than the fibre's diameter was needed. We used AES with two approaches (Figure 4.8). The first approach was to scan the electron beam over the lateral surface of individual fibres laying down and in intervals sputter away material with an ion gun and thereby create depth profiles. This approach gives very high spatial resolution in the transverse direction of the fibre, but it is time consuming and limited in how deep the sputtering can go. The second approach was to scan the electron beam across the cross-section of standing up carbon fibres. This makes it possible to analyse the entire diameter of the fibre in a short time, but the process is less stable as the fibre end has freedom to move and cause drift effects. In other words, the first approach is precise with a mechanically stable sample, but slow and limited in depth, while the second approach is fast and can cover the entire cross-section, but the sample is mechanically unstable.

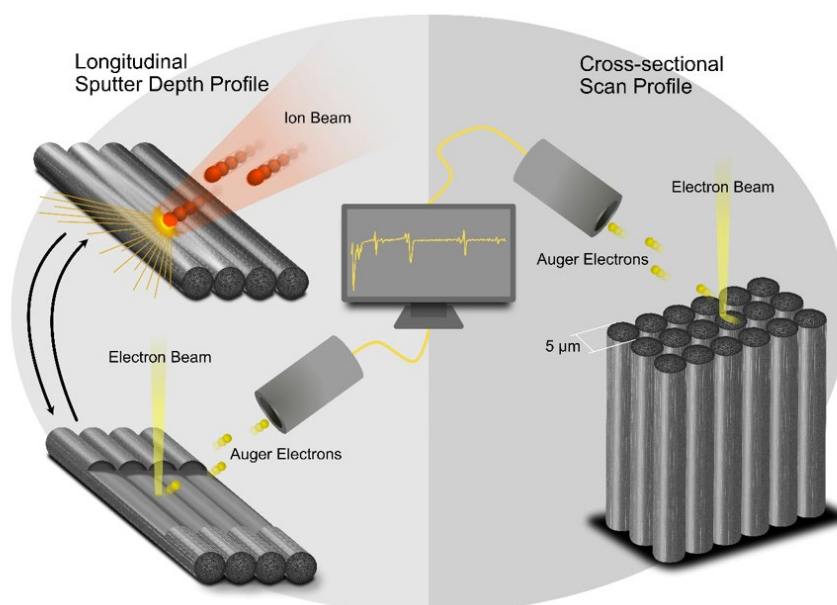


Figure 4.8: Schematic of the approaches to AES analysis of lithiated carbon fibre: fibres laying down, and fibres standing up. Reproduced from Ref. [82]. CC BY 4.0.

Experimentally the greatest challenge was to avoid charging and sample drift, without jeopardising resolution and signal-to-noise ratio. At the analysis point, the amount of influx of electrons must not excessively exceed the outflux, as not to induce build-up of charge, which can make the fibre mechanically sway or cause the migration of Li. In fact, at a beam current of 10 nA, small precipitates of presumably Li metal formed on the surface of the fibres. This artifact is of course unwanted for proper analysis, but we made use of the phenomena for peak identification, as can be read later in the text. The artifacts were circumvented with lower beam currents of 1 nA.

When analysing lithiated carbon fibres, the Li_{L} signal from XPS consists of one convoluted peak at 56 eV (Figure 4.9b), whereas Li_{KLL} signal from AES consists of three separate peaks at 35 eV, 45 eV, and 55 eV (Figure 4.9a). This is a rare case of spectral features of AES being easier to distinguish than XPS. However, at first, we did not know what these three Li_{KLL} peaks meant, and so had to identify what chemical state they represent.

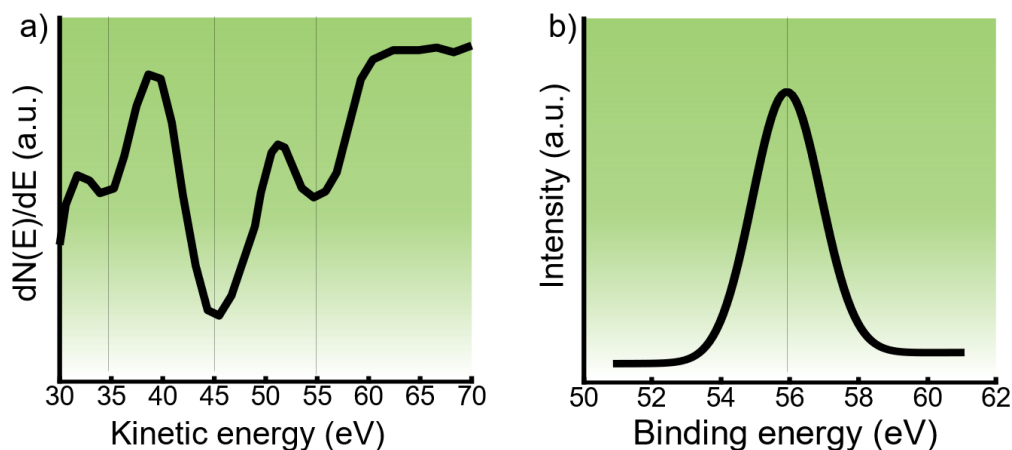


Figure 4.9: a) Li_{KLL} signal from AES on lithiated carbon fibres with its three peaks, and b) Li_{L} signal from XPS on lithiated carbon fibres. Adapted from Ref. [82]. CC BY 4.0.

We compared the evolution of the Li_{KLL} peaks over the depth profiles with the depth profiles of other elements. The Li_{KLL} 35 eV peak was found to follow the same trend in the depth profile on the lateral surface as the O_{KLL} at 510 eV (Figure 4.10a) and concluded to be associated with lithium bonded to oxygen (Li-O) [108]. The 45 eV peak followed the trend of the minor C_{KLL} peak at 260 eV (Figure 4.10b), which in other works has been associated with carbon bonded to metal, in this case lithium (C-Li) [109]. The 45 eV peak therefore represents lithium bonded to carbon (Li-C). However, the depth profile of the Li_{KLL} peak at 55 eV did not have the same trend as any of the other elements. A Li peak independent of other elements suggests elemental lithium (Li^0). We confirmed this by exposing the material to a beam current of 10 nA and simultaneously monitoring the SEM image and the AES spectra. At the same time as the Li metal precipitate formed on the surface the Li_{KLL} signal became dominated by the 55 eV peak (Figure 4.10c). Thus, we had a full understanding of how to interpret the Li_{KLL} signal.

The work highlighted the usefulness of AES in characterisation of Li-ion battery materials. It also prepared us to map the distribution of Li in carbon fibres for structural batteries.

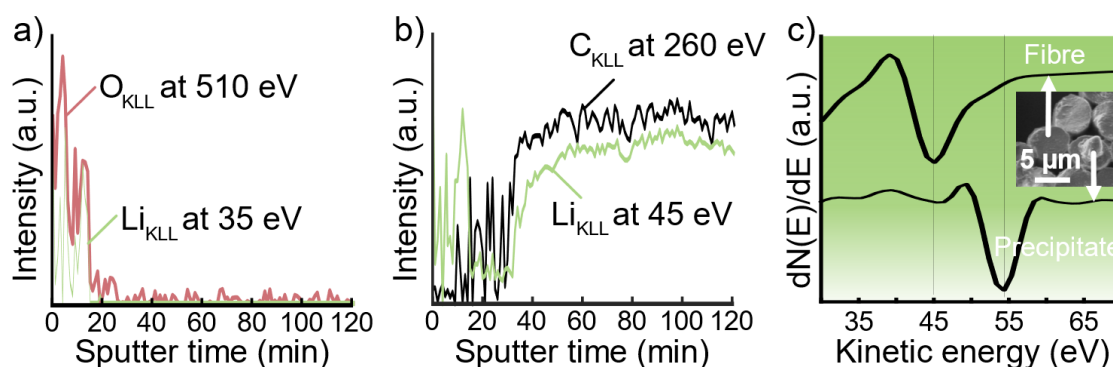


Figure 4.10: a) Depth profile of the 35 eV peak of Li_{KLL} and O_{KLL} . b) Depth profile of the 45 eV of Li_{KLL} and the 260 eV peak of C_{KLL} . c) Comparison of the Li_{KLL} signals of a lithiated carbon fibre and a Li metal precipitate. The inset is an SEM image of carbon fibre ends, with one of them exhibiting a Li metal precipitate induced by the electron beam. Adapted from Ref. [82]. CC BY 4.0.

4.2.2 Micro-scale mapping of Li: individual fibres

Much work by other studies had answered what the effects of Li insertion in carbon fibres are, such as: volumetric expansion, and mechanical degradation. However, not enough work had been done to answer how Li actually coordinates with the carbon fibres. Armed with an AES technique suitable for the task, we went looking for the answers.

The AES sputter depth profile of lithiated carbon fibres clearly showed two regions: the solid-electrolyte interphase (SEI) with fluctuating intensities and the carbon fibre with stable intensities (Figure 4.11). AES detected Li, P, F, O, and C in the SEI as it is made up of reaction products from LiPF_6 , $\text{OC}(\text{OCH}_3)_2$, and $(\text{CH}_2\text{O})_2\text{CO}$ from the electrolyte. In the fibre region only C and Li was detected. Small amounts of N were detected in uncycled carbon fibres, but with the introduction of Li, the relative amount of N fell below the detection limit of the instrument. We concluded that no co-insertion of F, P, or O, takes place in the fibres.

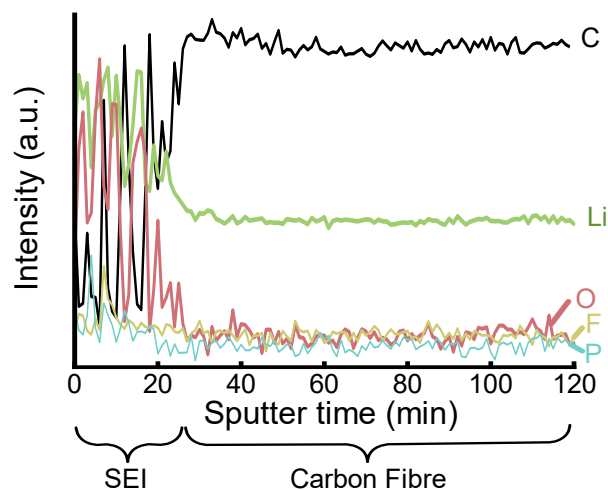


Figure 4.11: Depth profile of a lithiated carbon fibre. Adapted from Ref. [82]. CC BY 4.0.

When the Li_{KLL} signal was broken down to the three components, Li-O , Li-C , and Li^0 , the depth profile showed that various Li species are predominant at different depths (Figure 4.12a). In the SEI, all three are present, but in the fibre only Li-C is present. We generated depth profiles for four positions on three adjacent fibres to understand how the composition varies along the fibres and from fibre to fibre. Just looking at the individual fibre (4.12a-d), the SEI thickness is uniform along the fibre, as well as the Li concentration in the fibre. However, when the middle fibre (4.12e-h) was compared to the fibre to the left (4.12a-d) and to the right (4.12i-l), it was clear that not all fibres have the same SEI thickness, since the middle one had around double the thickness. Furthermore, this middle fibre also showed an intermittent region between SEI and fibre, where the concentration of Li^0 was particularly high. This is likely Li plating and can be detrimental to the cell as the build-up of trapped inactive Li will reduce the cell's capacity and eventually cause safety issues. Despite the different forms of SEI, all three fibres exhibited roughly the same concentration of Li. Apparently, the Li concentration is uniform both throughout the individual fibre and from fibre to fibre, but still the SEIs on the surface of the fibres are very different. So, even though the fibres store the same amount of energy, their different SEIs will likely make them perform differently during electrochemical cycling. This knowledge is useful in future design of structural batteries, as the plating should be avoided.

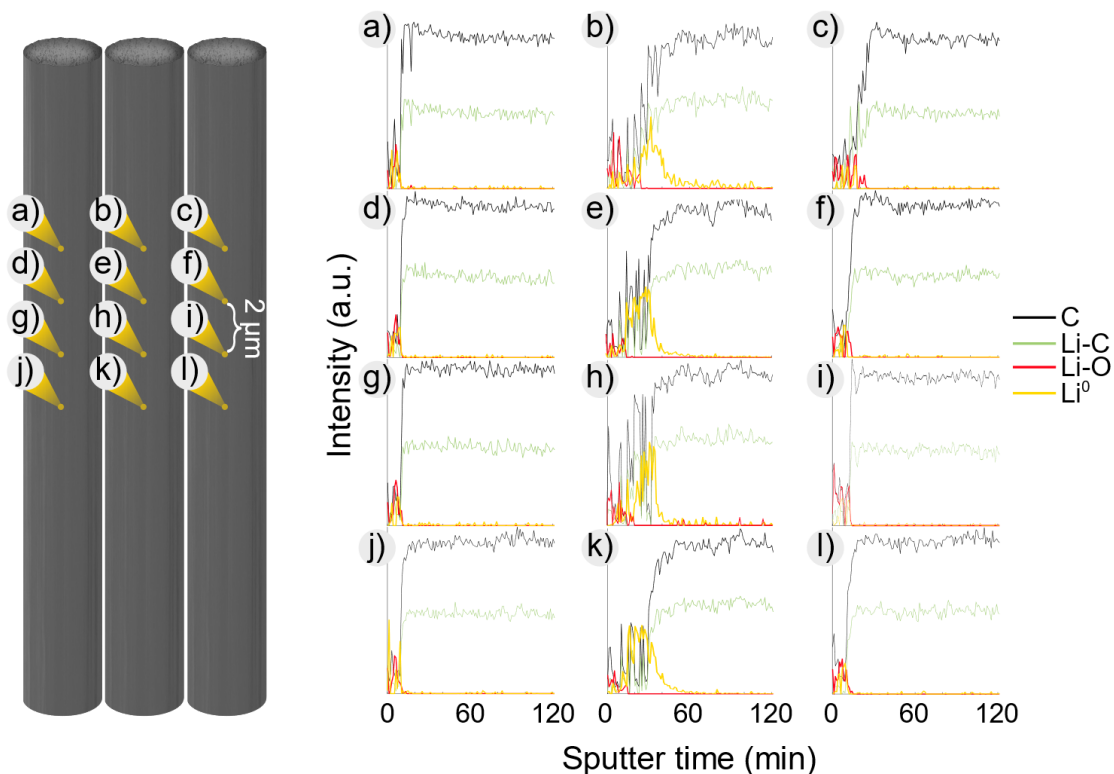


Figure 4.12: Depth profiles of three adjacent carbon fibres generated for four positions per fibre. Reproduced from Ref. [82]. CC BY 4.0.

Looking closer at only the interior of the fibres, we investigated different levels of lithiation and charge rates. Fibres lithiated slowly with a charge rate of 0.05C to 50% state of lithiation showed a uniform distribution of Li, which continued to be uniform when the same rate was used to bring the fibre to 100% state of lithiation (Figure 4.13a). However, comparing the C_{KLL} signal of 100% lithiated and 50% lithiated fibres, there were differences in the shape, where the fully lithiated fibre had a fine feature at 280 eV, while the half lithiated fibre did not (Figure 4.13b). This shape difference can be explained if the C_{KLL} signal is seen as a convolution of peaks from different bonds, σ and π bonds, in the carbon structure [110]. As Li intercalates between graphene layers [111], it donates an electron to the antibonding π^* band, which leads to a high energy feature around 280 eV. With intercalation occurring only in ordered domains of carbon, the presence of a fine feature at 280 eV suggests that at the later stages of lithiation, lithium is inserted in the ordered domains, while at lower states of lithiation it is inserted in disordered domains [112].

Finally, as we studied delithiated fibres, we saw that fibres slowly delithiated with a discharge rate of 0.05C were drained of Li to such a degree that the Li concentration fell below the detection limit of AES (Figure 4.13a). However, more rapid delithiation of 0.2C led to Li being retained inside the fibre, with larger quantities of trapped Li located near the centre of the fibre. This is possibly due to the skin-core microstructure of carbon fibres [67], [113], and the longer diffusion distance. Nevertheless, it can be concluded that increased discharge rate led to more trapped Li.

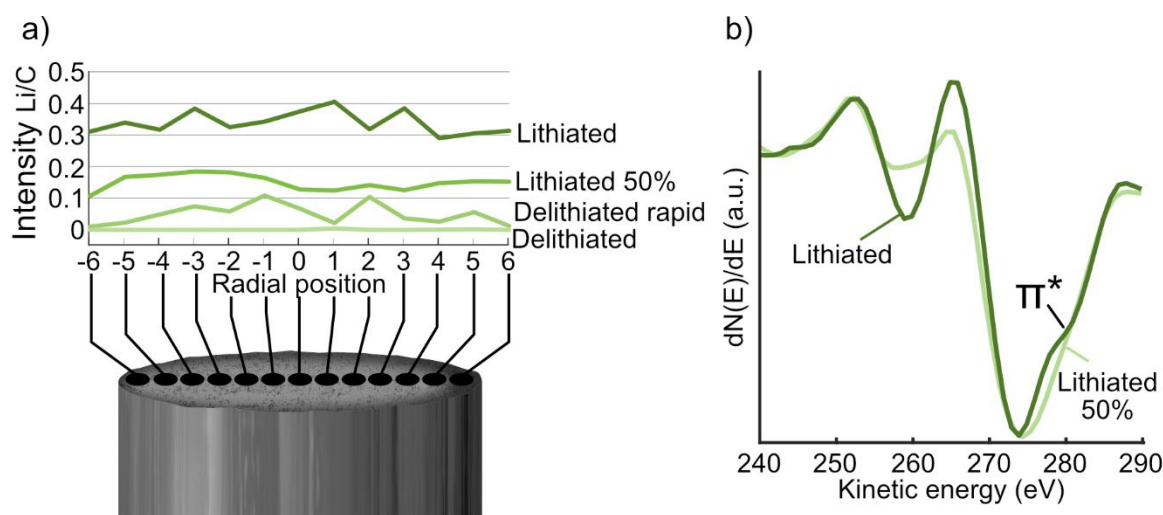


Fig. 4.13: a) The Li/C intensity ratio across the cross-sections of fully lithiated fibres, half-lithiated fibres, and completely delithiated fibres slow and fast. Comparison of the shape of C_{KLL} of fully lithiated and half-lithiated fibres, where the fully lithiated fibres show a fine structure feature representing the occupation of the π^* band. Adapted from Ref. [82]. CC BY 4.0.

4.2.3 Expanding APT methodology

The challenge of analysing lithiated carbon fibres with APT arises from the great difference between Li and C. Li is electrochemically reactive and highly mobile, while carbon fibres are physiochemically stable and exhibit semi-conductivity. In the atom probe, the electrostatic field penetrates deep into materials with lower conductivity. Thus, the field induces migration of Li towards the surface [114]. Since the field evaporation of $C \rightarrow C^+$ requires one of the strongest electrostatic fields (142 V/nm), whereas field evaporation of $Li \rightarrow Li^+$, only requires a tenth of that in field strength (14 V/nm), massive field evaporation of Li takes place first at low voltages, and later C is field evaporated at higher voltages. The specimen tip is in essence being *in situ* delithiated [115]. This phenomenon was manifested in the reconstruction as a cap of Li on a carbon fibre tip (Figure 4.14). Hence, the actual distribution of Li was distorted by the field, and to properly investigate the lithiated carbon fibre, this artifact needed to be mitigated.

We shielded the APT tips from the electrostatic field by coating them with chromium (Cr). To avoid exposure to ambient air, the tips were coated inside a FIB/SEM in accordance with the method of Woods et al. [116]. A lamella of Cr with a semi-circle cut-out at one end was held by a micromanipulator and the APT tip was centred in the cut-out (Figure 4.15a). With the ion-beam, Cr was sputter off the lamella so that it was redeposited on the APT tip. The subsequent reconstruction showed no massive evaporation of Li (Figure 4.15b), and the Li distribution was retained.

This work demonstrates that it is possible to prevent massive evaporation of Li in lithiated carbon fibres during APT analysis. Furthermore, the work equipped us with the opportunity to investigate the atomic distribution of Li in lithiated carbon fibres.

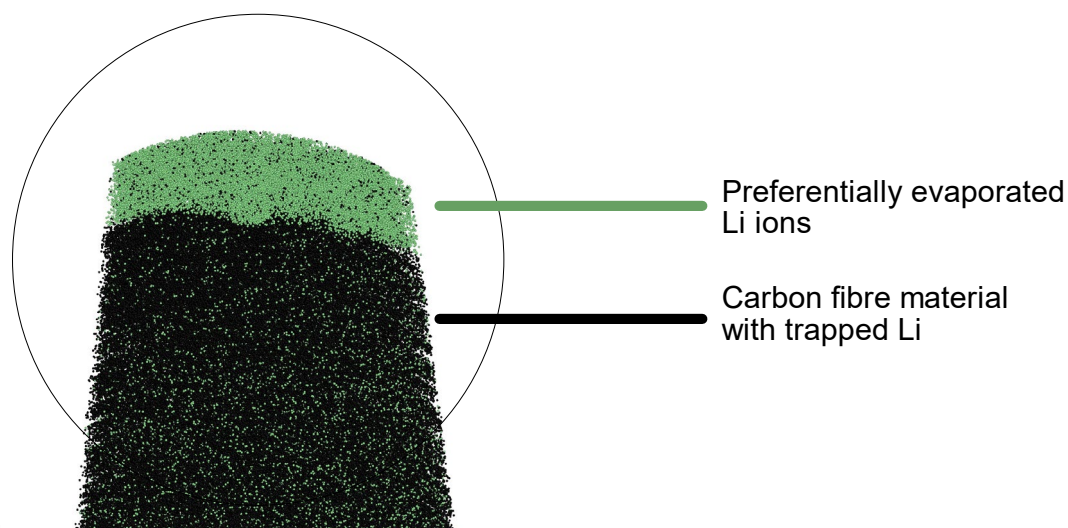


Figure 4.14: Reconstruction of lithiated carbon fibre. Green dots represent Li and black dots C.

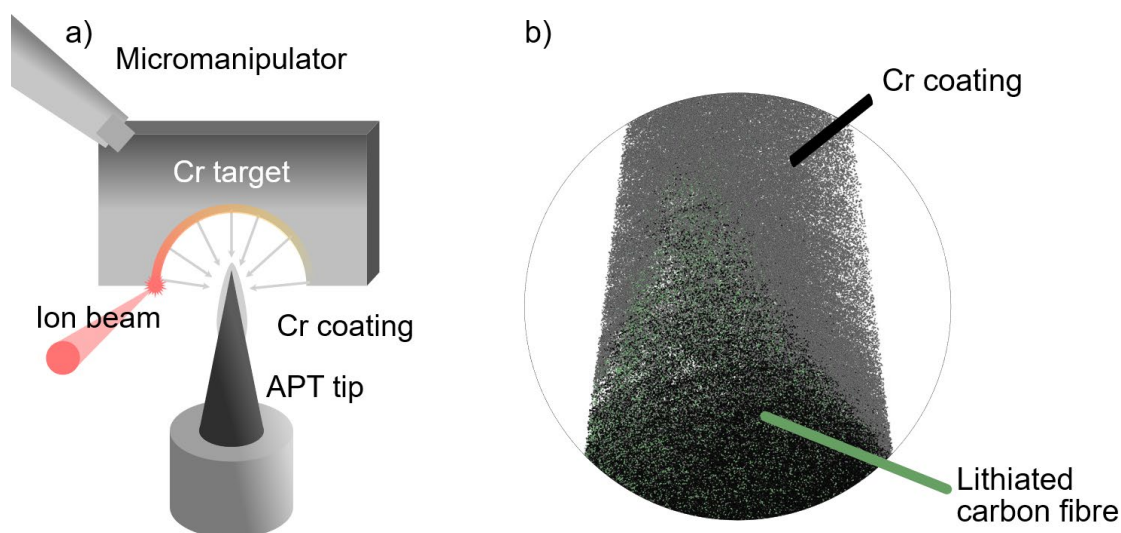


Figure 4.15: a) Schematic of Cr coating procedure. An ion-beam directed at a pre-cut Cr target sputters away Cr to be redeposited on an APT tip. b) Reconstruction of Cr coated lithiated carbon fibre. Grey dots represent Cr, green dots Li, and black dots C.

4.2.4 Nano-scale mapping of Li: individual atoms

At the final stage of this work, we had built up understanding of carbon fibres with electron spectroscopy techniques and grasped how carbon fibres ought to be investigated with APT. We were ready to answer how Li is distributed on the atomic scale in lithiated carbon fibres.

The spectra for coated lithiated carbon fibres were even more complex than the spectra of uncycled carbon fibres (Figure 4.16) as the addition of Li (Table 4.3) from the electrochemical cycling and Cr (Table 4.4) from the coating introduces new peaks, of which several overlapped with each other and the spectrum from the carbon fibre itself. To minimize the influence of the Cr coating, we extracted a cylinder-shaped region of interest in the centre of the carbon fibre away from the coating. However, Cr peaks were still

detected, which indicated that the sputtered material was implanted into the carbonaceous material. The spectrum was deconvoluted based on the isotopic abundance C and Cr. The residual ions were assigned as Li related.

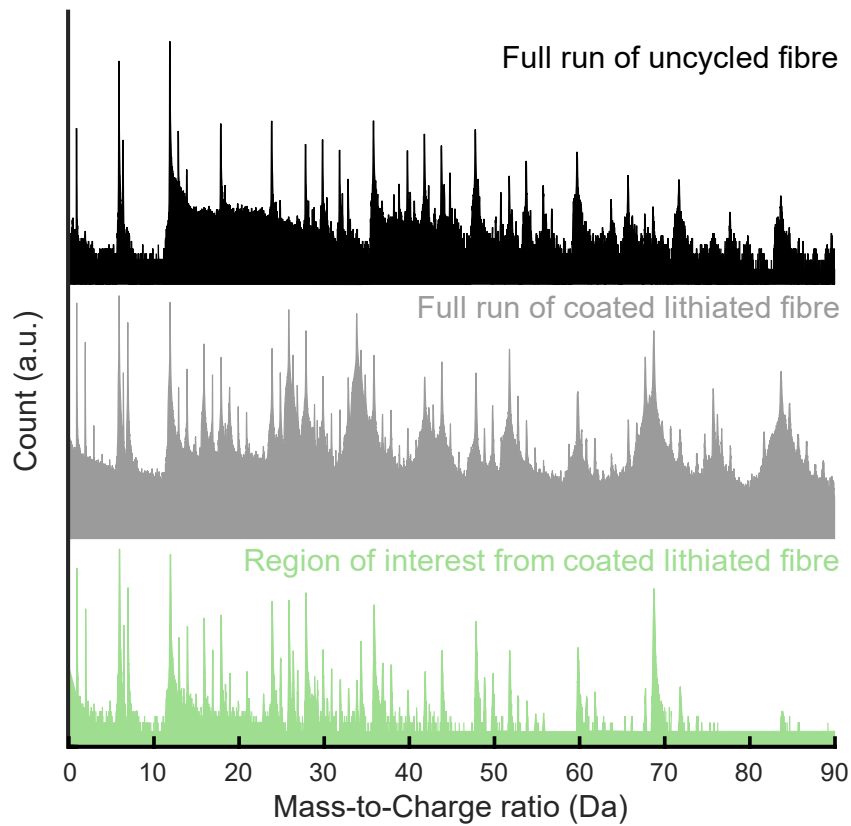


Figure 4.16: Mass spectra of uncycled carbon fibre (upper), Cr coated lithiated fibre (middle), and region of interest extracted from centre of Cr coated lithiated fibre (lower).

Table 4.3: Possible mass-to-charge peaks related to Li. Peaks marked with green tiles are encountered in the mass spectra of lithiated T800 carbon fibres.

	x=1 [+]	x=1 [2+]	x=2 [+]	x=2 [2+]	x=3 [+]	x=3 [2+]	x=4 [+]	x=4 [2+]
Li_x	7	3.5	14	7				
LiC_x	19	9.5	31	15.5	43	21.5	55	27.5
Li_2C_x	26	13	38	19	50	25	62	31
Li_xN	21	10.5	28	14				
Li_xO	23	11.5	30	15				
Li_xNO	37	18.5	44	22				
Li_xCO	35	17.5	42	21				
Li_xCNO	49	24.5	56	28				
Li_xCN	33	16.5	40	20				

Table 4.4: Encountered mass-to-charge peaks related to Cr.

	^{50}Cr	^{52}Cr	^{53}Cr	^{54}Cr
Cr[2+]	25	26	26.5	27
Cr[+]	50	52	53	54
CrO[2+]	33	34	34.5	35
CrO[+]	66	68	69	70
CrO ₂ [2+]	41	42	42.5	43
CrO ₂ [+]	82	84	85	86
Cr ₂ O[2+]	59	60	60.5	61
Cr ₂ O ₂ [2+]	67	68	68.5	69
Cr ₂ O ₃ [2+]	75	76	76.5	77

After deconvolution the elemental compositions of lithiated and delithiated fibres were calculated (Table 4.3). The Li concentration in delithiated T800 carbon fibres was measured to 1.6 at%, which meant that there was indeed Li trapped inside the fibres after delithiation. This is a significant amount and corresponds to ~35 mAh/g of lost capacity in a T800 carbon fibre. The total amount of lost capacity was calculated to ~155 mAh/g based on the capacity of the first and last cycle, meaning that ~23% of the capacity loss originated from Li trapped in the fibre. The expected Li concentration in lithiated T800 carbon fibres was 9.9 at% excluding any trapped Li. With the measured amount of trapped Li, the expected concentration was thus 11.5 at%. However, the measured Li concentration in lithiated fibres was 9.1 at%.

Table 4.3: Composition of uncycled, delithiated, and delithiated carbon fibres.

at%	C	Li	N	O
Uncycled	96.6	-	2.7	0.7
Delithiated	94.4	1.6	2.4	1.6
Lithiated	86.6	9.1	2.9	1.4

Deconvolution based on natural isotopic abundance can be used to calculate more accurate elemental compositions by estimating how large parts of a given mass-to-charge peak corresponds to an ion species. However, it is not able to differentiate in overlapping peaks which one of the collected ions corresponds to which overlapping ion species. Therefore, the information on the spatial distribution of ions in an overlapping peak is at best muddled, and in worst case completely obscured. Hence, analysis of spatial distribution is usually conducted based on only ions from non-overlapping peaks, and their distribution is assumed to be representative. Unfortunately, all peaks containing Li experienced potential overlaps. The largest source of Li in the spectrum came from the peak at 7 Da, which largely overlapped with a peak containing N. The mass-to-charge ratios for Li^+ and N^{2+} differs slightly: 7.02 Da, and 7.00 Da, respectively [117]. This was observed as a small separation in peak position (Figure 4.17). However, the partial overlap still meant unreliable spatial information. Typically, a division between the peaks is introduced and ions are assigned based on whether their mass-to-charge ratio falls left or right of the division (Figure 4.17a). Still, some ions will be incorrectly assigned with this rather blunt approach. We instead used a more elegant approach of deconvolution based of the different

evaporation conditions that Li^+ and N^{2+} experiences. By superimposing spectra of single and multi-hits, we revealed that the former ion was detected as single hit ions, while the latter was detected as multiple hit ions (Figure 4.17b). Consequently, we deconvoluted the 7 Da peak based on single and multi-hits. With only single hit ions from the 7 Da peak we had intact spatial information for Li.

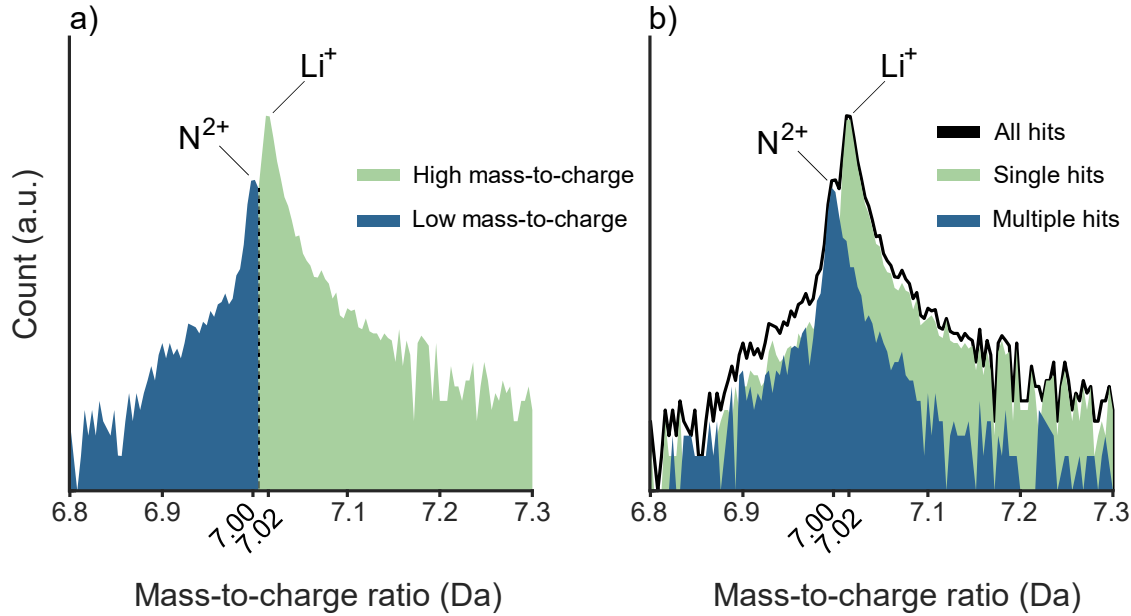


Figure 4.17: Deconvolution of the 7 Da peak based on a) mass-to-charge ratio, and b) single/multi-hits.

Since no visible agglomerations of Li were identified by just observing the reconstructions, more detailed analysis was required. We employed frequency distribution analysis of the data sets from delithiated and lithiated carbon fibres (Figure 4.17). The data sets were divided into bins of 100 ions. Each bin's composition was calculated and histograms of the number of encountered Li concentrations were generated. Binomial distributions were projected on the histograms. The binomial distribution represents the frequency distribution of a random system, and is given by:

$$F(i) = n_F \frac{N_b!}{i!(N_b-i)!} p^i q^{N_b-i}, \quad (\text{Equation 4.2})$$

where i is the number of the solute atoms, $F(i)$ is the expected number of bins with i atoms, N_b is the total number of atoms, n_F is the total number of bins, p is the probability of encountering the solute atom (i.e. total concentration of the solute atom), and q is the probability of not encountering the solute atom (i.e. $q = p - 1$). In other words, the closer the measured frequency distribution follows the binomial distribution, the closer the investigated atoms are random distribution. The adherence to the binomial distribution can be quantified with the Pearson coefficient, μ , which is a number decreasing from 1 to 0 with increasing adherence [118]. The frequency distribution analysis of Li in delithiated carbon fibres gave a Pearson coefficient of $\mu = 0.15$, which indicated a random distribution

of Li. For lithiated carbon fibres, though, the Pearson coefficient was $\mu = 0.49$, which pointed to a much more agglomerated distribution compared to delithiated fibres.

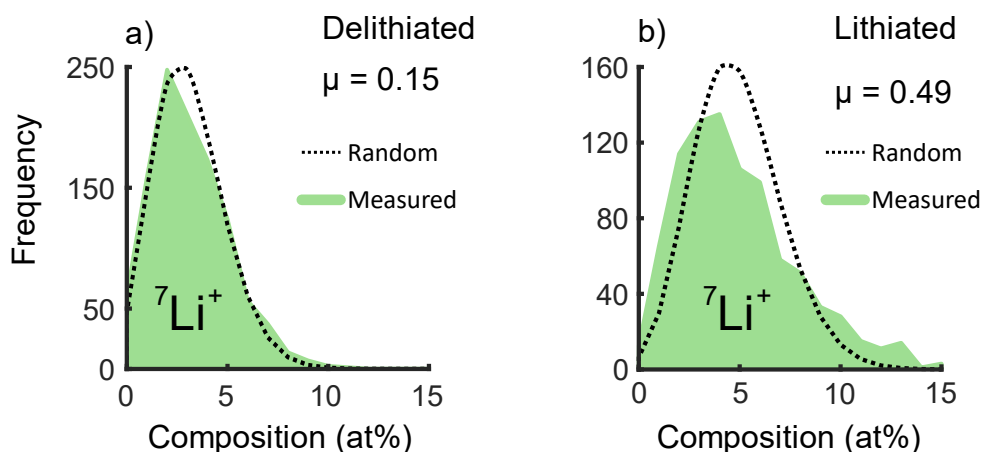


Figure 4.18: Frequency distribution diagram of Li in a) delithiated and b) lithiated carbon fibres.

Since we previously had identified with HAXPES that pyridinic and pyrrolic N are connected to enhanced electrochemical performance, we investigated whether the distribution of N in carbon fibres had any effect on the distribution of Li and could explain the agglomeration of Li in lithiated fibres. We used nearest neighbour analysis [119], where the distance in the APT reconstruction from each Li atom to its closest N atom was measured, and the plotted in a histogram (Figure 4.19). The distribution of distances separating each Li to its closest N followed a random distribution for both delithiated and delithiated carbon fibres. This means that the distribution of Li in a carbon fibre is independent of the distribution of N. It does not, however, necessarily dispute the effect N heteroatoms has on the electrochemical performance of carbon fibres, as they can induce defects in the carbon structure that allows for easier ion transport in the fibre, and thus improve the electrode properties.

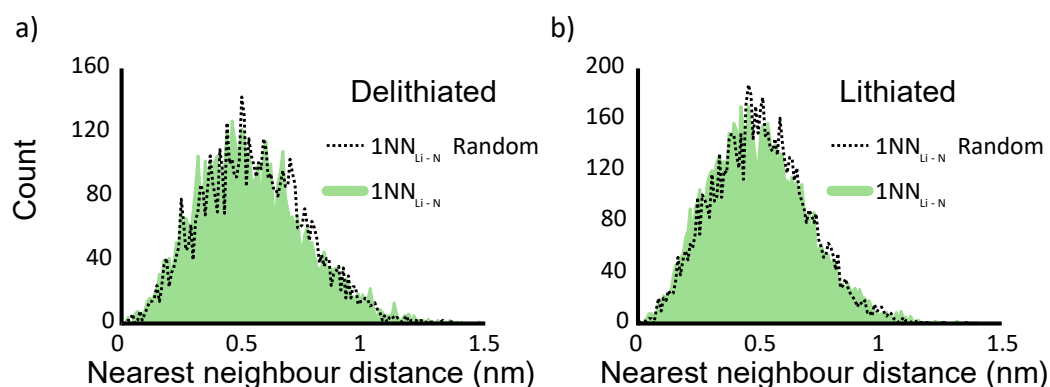


Figure 4.19: Nearest neighbour analysis of the distance between Li and nearest N in a) delithiated, and b) lithiated carbon fibres.

Since the distribution of N heteroatoms is unable to explain the agglomeration of Li in lithiated carbon fibres, the agglomeration is most likely an effect of the crystalline and amorphous domains in the carbon fibre. Thus, it can be assumed that the frequency distribution analysis indicates that one of the two domains contain more Li, whereas the other contains less Li. We were unable to discern with APT in what domain Li is most abundant, but given that our AES study identified the amorphous domain to be first to experience Li insertion during the lithiation process, the amorphous domain is presumably also the domain most easily accessed by Li. Conversely, the crystallites accept less Li. This agrees with the fact that carbon fibres with larger crystallites have lower electrochemical capacity [64]. The turbostratic stacking of the graphene layers inhibits Li insertion [19]. Since the crystallites are the limiting factor, we recognise them as the prime focus for improving the electrochemical capacity of carbon fibres.

The design of crystallites can entail two different approaches. The first approach is to reduce the obstructing effect of the crystallites by making the crystallites smaller. Making the amorphous domain a larger portion should give higher capacity, but at the same time, it risks jeopardising modulus and conductivity [52], [56]. The other approach is instead focused on enhancing the crystallites rather than diminishing their obstructing effect. Efforts to make the stacking of graphene layers less turbostratic and more graphitic should lead to increased electrochemical capacity. Nonetheless, graphitisation is usually accompanied by growth of the crystallites, which will intrude on the advantageous amorphous domain. Furthermore, fully graphitic stacking in carbon fibres can be difficult. The level of graphitisation in a carbon material can be gauged based on how close the interplanar spacing between the graphene layers is to that of pure graphite at 3.35 Å [52]. However, highly ordered M60J carbon fibres that have experienced very high final heat treatment temperature (1800-3000 °C) only reach 3.47 Å in interplanar spacing [64], which is far from that of graphite, and illustrates the difficulty for the crystallites to reach graphitic stacking. Still, regardless of it being difficult, it would be advantageous with carbon fibres exhibiting large amounts of amorphous domains interspersed by tiny but highly graphitic crystallites.

This work was the culmination of persistent efforts to uncover, with increasing spatial resolution, the carbon fibre at its different electrochemical states. We identified further pathways for improvement in carbon fibres for multifunctional purposes. Firstly, the significant entrapment of Li inside the fibre should be suppressed, and thereby parts of the capacity fade can be eliminated. Secondly, the crystallites should be boosted to accommodate more Li to improve the overall capacity. Much work of course remains, but this work and this thesis as a whole have opened several doors to elevating the performance of carbon fibres in structural batteries.

5 Summary of appended papers

Paper I: Best Practice for Analysis of Carbon Fibres by Atom Probe Tomography

In this paper, we propose a best practice for how to conduct APT on the challenging material of carbon fibres. Since so limited amount of work on the subject had been done before, this paper became the first guide for APT on carbon fibres. It discusses approaches to enhance experimental results and increase data analysis accuracy. This includes how to improve mass resolution, increase data size, identify mass-to-charge peaks, deconvolute overlapping peaks, and reduce multiple hit events. The paper unlocks research opportunities to increase the understanding of carbon fibres and other carbonaceous materials using APT.

Paper II: Mapping Nitrogen Heteroatoms in Carbon Fibres using Atom Probe Tomography and Photoelectron Spectroscopy

In this paper, we use APT and HAXPES to investigate three types of PAN-based carbon fibres and their configuration and distribution of N heteroatoms. The electrochemical performance of carbon materials has been proved to enhance with N-doping. With N being an inherent constituent of PAN-based carbon fibres, it is therefore interesting to understand how it affects their properties. N is only found in the fibres with less ordered microstructure. In these fibres, it is found that N distributes uniformly, but N configurations influence the fibres properties. Pyridinic and pyrrolic-N are concluded to lead to increased electrochemical performance. The paper shows that N heteroatoms are an important design parameter for tuning the multifunctionality of carbon fibres.

Paper III: Lithiated Carbon Fibres for Structural Batteries Characterised with Auger Electron Spectroscopy

In this paper, we use AES and XPS to analyse the distribution of Li in carbon fibres from electrochemically cycled structural batteries. We present several findings: individual fibres have different thicknesses of SEI; some fibres experience Li plating; Li is inserted in disordered domains of the fibres at early stages of lithiation and in ordered domains at later stages; and charge rate affects the amount of trapped lithium. The paper proves AES to be a powerful tool for analysing Li in carbon materials, provides insights of the interaction between lithium and carbon fibres that can help further develop the field of structural batteries.

Paper IV: Suppressing lithium migration in carbon fiber negative electrode during atom probe tomography analysis

In this paper, we build upon the best practice proposed in Paper I, and demonstrate a method to study Li in the carbon fibres. The different evaporation behaviours of C and Li is shown to induce massive evaporation of Li during APT analysis. The massive evaporation is identified as the effect of deep penetration of the electrostatic field into the semi-conductive carbon fibres. We attempt to shield the APT tips of lithiated carbon fibre from the field by coating them with Cr coating, and thereby suppress the massive evaporation. The effect of the Cr coating on mass resolution and atomic composition is discussed. The paper shows that lithiated carbon fibres can be properly analysed with APT if the specimens are shielded from the electrostatic field.

Paper V: Unravelling Lithium in Electrochemically Active Carbon Fibres with Atom Probe Tomography

In this paper, we use APT based on the knowledge gained from Paper I and Paper IV to analyse the atomic distribution of Li in lithiated carbon fibres. We find that a significant part of the electrochemical capacity fade in carbon fibres is due to Li trapped in the microstructure of the carbon fibres. This trapped Li is uniformly distributed in delithiated carbon fibres, but in fully lithiated fibres, Li agglomerates. Threads from Paper II are further investigated as we analyse N heteroatoms' influence on the distribution of Li. Li proves to distribute independently of N, but the importance of N for enhanced electrochemical performance is not rejected. The paper highlights that design of new multifunctional carbon fibres should focus on modifying the crystallites and preventing Li entrapment.

6 Outlook

This thesis is merely a step towards fully understanding and harnessing the multifunctionality of carbon fibres to further develop structural batteries. A wide array of research avenues remains to be explored, of which a few follows here.

Design and synthesis of multifunctional carbon fibres

One can only get so far by investigating existing carbon fibre types. The hypothesis of how to make a carbon fibre perform better electrochemically must be tested by designing new fibre types, manufacturing them, and measuring their properties, without the ambiguity of the details of manufacturing processes behind commercial carbon fibres. This will expand the understanding of the relationship between manufacturing parameters, microstructure, and multifunctionality. Additionally, the countless small variations between different types of commercial carbon fibres, even within the same category, blurs causal relations. It is therefore desirable to investigate, for instance, how only altering one process parameter affects the multifunctionality of carbon fibres. Ideally, a closed loop is established where design adjustments are implemented to manufacture fibres that are characterised and inform new design adjustments.

TEM of lithiated carbon fibres

In this thesis there is a significant leap in length scale between APT and AES. Assumptions based on interpolation can of course be made, however, bridging the gap with other characterisation techniques is needed to further understand Li in carbon fibres. Transmission electron microscopy (TEM) coupled with electron energy loss spectroscopy (EELS) on lithiated carbon fibres can reveal the distribution of Li in 2D and also provide information on chemical states, but at a larger scale than APT. TEM/EELS can therefore potentially elucidate more clearly how and at what stage Li inserts in crystalline and amorphous domains.

APT of SEI on carbon fibres

The multifunctional carbon fibre is a part of the larger system of the structural battery. Hence, further research must seek to understand the interface between fibre and other constituents. Building on the techniques used in this thesis, it is natural to use APT to investigate the boundary between the fibre and the electrolyte: the solid-electrolyte interphase (SEI). Dried SEI can of course be investigated with APT, but eventually the wet state must also be preserved and studied. With this aspiration further challenges present

themselves. To analyse liquids with APT, cryo-specimen preparations are needed. By freezing the samples, dynamic conditions may be captured.

In-situ observation of carbon fibre electrode

In terms of electrochemical processes, all the previously suggested experiments try to explain dynamic processes but are ex-situ in nature. To properly capture the dynamic processes the carbon fibres experience, in-situ testing is essential. FIB/SEM equipped with micromanipulators and potentiostats can record in real time the dynamics on lithiation and delithiation of specially constructed cells with carbon fibre electrodes. The micromanipulators or miniature mechanical testing rigs can induce mechanical loads while the potentiostat provides the electrochemical load. After the in-situ experiments have been performed FIB, can reveal buried features and through serial milling and combination of consecutive 2D images create 3D information of the fibres and its surroundings.

References

- [1] S. L. H.-O. Pörtner, D.C. Roberts, M. Tignor, E.S. Poloczanska, K. Mintenbeck, A. Alegría, M. Craig and B. R. S. Löschke, V. Möller, A. Okem, “PCC, 2022: Climate Change 2022: Impacts, Adaptation and Vulnerability. Contribution of Working Group II to the Sixth Assessment Report of the Intergovernmental Panel on Climate ChangeNo Title,” Cambridge, UK and New York, NY, USA, 2022.
- [2] M. Woodward *et al.*, “Electric vehicles - Setting a course for 2030,” 2020.
- [3] A. D. B. L. Ferreira, P. R. O. Nóvoa, and A. T. Marques, “Multifunctional Material Systems: A state-of-the-art review,” *Compos. Struct.*, vol. 151, pp. 3–35, 2016.
- [4] A. Lendlein and R. S. Trask, “Multifunctional materials: Concepts, function-structure relationships, knowledge-based design, translational materials research,” *Multifunct. Mater.*, vol. 1, no. 1, 2018.
- [5] L. E. Asp and E. S. Greenhalgh, “Structural power composites,” *Compos. Sci. Technol.*, vol. 101, pp. 41–61, 2014.
- [6] L. E. Asp *et al.*, “A Structural Battery and its Multifunctional Performance,” *Adv. Energy Sustain. Res.*, vol. 2000093, 2021.
- [7] G. J. H. Lim, K. K. Chan, N. A. A. Sutrisnoh, and M. Srinivasan, “Design of structural batteries: carbon fibers and alternative form factors,” *Mater. Today Sustain.*, vol. 20, p. 100252, 2022.
- [8] H. Berg, *Batteries for Electric Vehicles*. Cambridge University Press, 2015.
- [9] B. Dunn, H. Kamath, and J. M. Tarascon, “Electrical energy storage for the grid: A battery of choices,” *Science (80-.)*, vol. 334, no. 6058, pp. 928–935, 2011.
- [10] R. Schmuck, R. Wagner, G. Hörpel, T. Placke, and M. Winter, “Performance and cost of materials for lithium-based rechargeable automotive batteries,” *Nat. Energy*, vol. 3, no. 4, pp. 267–278, 2018.
- [11] Z. P. Cano *et al.*, “Batteries and fuel cells for emerging electric vehicle markets,” *Nat. Energy*, vol. 3, no. 4, pp. 279–289, 2018.
- [12] J. B. Goodenough and K. S. Park, “The Li-ion rechargeable battery: A perspective,” *J. Am. Chem. Soc.*, vol. 135, no. 4, pp. 1167–1176, 2013.

- [13] M. Winter, B. Barnett, and K. Xu, “Before Li Ion Batteries,” *Chem. Rev.*, vol. 118, no. 23, pp. 11433–11456, 2018.
- [14] M. Armand and J.-M. Tarascon, “Building better batteries,” *Nature*, vol. 451, no. 7179, pp. 652–657, Feb. 2008.
- [15] R. Yazami and P. Touzain, “A reversible graphite-lithium negative electrode for electrochemical generators,” *J. Power Sources*, vol. 9, no. 3, pp. 365–371, Jan. 1983.
- [16] J. Asenbauer, T. Eisenmann, M. Kuenzel, A. Kazzazi, Z. Chen, and D. Bresser, “The success story of graphite as a lithium-ion anode material-fundamentals, remaining challenges, and recent developments including silicon (oxide) composites,” *Sustain. Energy Fuels*, vol. 4, no. 11, pp. 5387–5416, 2020.
- [17] H. Zhang, Y. Yang, D. Ren, L. Wang, and X. He, “Graphite as anode materials: Fundamental mechanism, recent progress and advances,” *Energy Storage Mater.*, vol. 36, no. October 2020, pp. 147–170, 2021.
- [18] Q. Liu *et al.*, “Kinetically Determined Phase Transition from Stage II (LiC₁₂) to Stage i (LiC₆) in a Graphite Anode for Li-Ion Batteries,” *J. Phys. Chem. Lett.*, vol. 9, no. 18, pp. 5567–5573, 2018.
- [19] J. R. Dahn, T. Zheng, Y. Liu, and J. S. Xue, “Mechanisms for Lithium Insertion in Carbonaceous Materials,” *Science (80-.)*, vol. 270, no. 5236, pp. 590–593, Oct. 1995.
- [20] M. Endo and Y. Ahm Kim, *Applications of Advanced Carbon Materials to the Lithium Ion Secondary Battery*. Elsevier Ltd, 2003.
- [21] M. Inagaki, M. Toyoda, Y. Soneda, and T. Morishita, “Nitrogen-doped carbon materials,” *Carbon N. Y.*, vol. 132, pp. 104–140, 2018.
- [22] A. L. M. Reddy, A. Srivastava, S. R. Gowda, H. Gullapalli, M. Dubey, and P. M. Ajayan, “Synthesis of nitrogen-doped graphene films for lithium battery application,” *ACS Nano*, vol. 4, no. 11, pp. 6337–6342, 2010.
- [23] P. Han *et al.*, “Nitrogen-doping of chemically reduced mesocarbon microbead oxide for the improved performance of lithium ion batteries,” *Carbon N. Y.*, vol. 50, no. 3, pp. 1355–1362, 2012.
- [24] S. J. An, J. Li, C. Daniel, D. Mohanty, S. Nagpure, and D. L. Wood, “The state of understanding of the lithium-ion-battery graphite solid electrolyte interphase (SEI) and its relationship to formation cycling,” *Carbon N. Y.*, vol. 105, pp. 52–76, 2016.
- [25] T. R. Jow, S. A. Delp, J. L. Allen, J.-P. Jones, and M. C. Smart, “Factors Limiting Li + Charge Transfer Kinetics in Li-Ion Batteries,” *J. Electrochem. Soc.*, vol. 165, no. 2, pp. A361–A367, 2018.
- [26] G. M. Veith, M. Doucet, R. L. Sacci, B. Vacaliuc, J. K. Baldwin, and J. F. Browning, “Determination of the Solid Electrolyte Interphase Structure Grown on a Silicon Electrode Using a Fluoroethylene Carbonate Additive,” *Sci. Rep.*, vol. 7,

- no. 1, pp. 1–15, 2017.
- [27] Y. Fang, A. J. Smith, R. W. Lindström, G. Lindbergh, and I. Furó, “Quantifying lithium lost to plating and formation of the solid-electrolyte interphase in graphite and commercial battery components,” *Appl. Mater. Today*, vol. 28, no. March, 2022.
 - [28] X. Lin, K. Khosravinia, X. Hu, J. Li, and W. Lu, “Lithium Plating Mechanism, Detection, and Mitigation in Lithium-Ion Batteries,” *Prog. Energy Combust. Sci.*, vol. 87, no. July, 2021.
 - [29] A. J. Smith *et al.*, “Localized lithium plating under mild cycling conditions in high-energy lithium-ion batteries,” *J. Power Sources*, vol. 573, no. January, 2023.
 - [30] B. D. Agarwal, L. J. Broutman, and K. Chandrashekhara, *Analysis and performance of fiber composites*, 4th ed. John Wiley & Sons, Inc., 2018.
 - [31] L. E. Asp, M. Johansson, G. Lindbergh, J. Xu, and D. Zenkert, “Structural battery composites: a review,” *Funct. Compos. Struct.*, vol. 1, no. 4, 2019.
 - [32] T. Jin, G. Singer, K. Liang, and Y. Yang, “Structural batteries: Advances, challenges and perspectives,” *Mater. Today*, 2022.
 - [33] J. Hagberg *et al.*, “Lithium iron phosphate coated carbon fiber electrodes for structural lithium ion batteries,” *Compos. Sci. Technol.*, vol. 162, no. April, pp. 235–243, 2018.
 - [34] J. S. Sanchez, J. Xu, Z. Xia, J. Sun, L. E. Asp, and V. Palermo, “Electrophoretic coating of LiFePO₄/Graphene oxide on carbon fibers as cathode electrodes for structural lithium ion batteries,” *Compos. Sci. Technol.*, vol. 208, no. March, p. 108768, 2021.
 - [35] N. Ihrner, W. Johannisson, F. Sieland, D. Zenkert, and M. Johansson, “Structural lithium ion battery electrolytes: Via reaction induced phase-separation,” *J. Mater. Chem. A*, vol. 5, no. 48, pp. 25652–25659, 2017.
 - [36] L. M. Schneider, N. Ihrner, D. Zenkert, and M. Johansson, “Bicontinuous Electrolytes via Thermally Initiated Polymerization for Structural Lithium Ion Batteries,” *ACS Appl. Energy Mater.*, vol. 2, no. 6, pp. 4362–4369, 2019.
 - [37] E. D. Wetzel, “Reducing weight: Multifunctional composites integrate power, communications, and structure,” *AMPTIAC Q.*, vol. 8, no. 4, pp. 91–95, 2004.
 - [38] E. L. Wong, D. M. Baechle, K. Xu, R. H. Carter, J. F. Snyder, and E. D. Wetzel, “Design and Processing of Structural Composite Batteries,” *Proc. Soc. Adv. Mater. Process Eng.*, 2007.
 - [39] J. F. Snyder, D. J. O’Brien, D. M. Baechle, D. E. Mattson, and E. D. Wetzel, “Structural composite capacitors, supercapacitors, and batteries for U.S. Army applications,” *Proc. ASME Conf. Smart Mater. Adapt. Struct. Intell. Syst. SMASIS2008*, vol. 1, pp. 1–8, 2008.

- [40] E. D. Wetzel, D. J. O. Brien, J. F. Snyder, R. H. Carter, and J. T. South, "Multifunctional Structural Power and Energy Composites for U.S Army Applications," *Multifunct. Struct. / Integr. Sensors Antennas*, no. 2006, pp. 2–14, 2006.
- [41] P. Liu, E. Sherman, and A. Jacobsen, "Design and fabrication of multifunctional structural batteries," *Journal of Power Sources*, vol. 189, pp. 646–650, 2009.
- [42] K. Moyer *et al.*, "Carbon fiber reinforced structural lithium-ion battery composite: Multifunctional power integration for CubeSats," *Energy Storage Mater.*, vol. 24, no. April 2019, pp. 676–681, 2020.
- [43] J. Xu *et al.*, "A multicell structural battery composite laminate," *EcoMat*, vol. 4, no. 3, pp. 1–11, 2022.
- [44] M. S. Siraj *et al.*, "Advancing Structural Battery Composites: Robust Manufacturing for Enhanced and Consistent Multifunctional Performance," *Adv. Energy Sustain. Res.*, vol. 2300109, 2023.
- [45] J. F. Snyder, E. L. Wong, and C. W. Hubbard, "Evaluation of Commercially Available Carbon Fibers, Fabrics, and Papers for Potential Use in Multifunctional Energy Storage Applications," *J. Electrochem. Soc.*, vol. 156, no. 3, p. A215, 2009.
- [46] J. Hagberg, S. Leijonmarck, and G. Lindbergh, "High Precision Coulometry of Commercial PAN-Based Carbon Fibers as Electrodes in Structural Batteries," *J. Electrochem. Soc.*, vol. 163, no. 8, pp. A1790–A1797, 2016.
- [47] J. Xu *et al.*, "Effect of tension during stabilization on carbon fiber multifunctionality for structural battery composites," *Carbon N. Y.*, vol. 209, no. March, p. 117982, Jun. 2023.
- [48] M. Sauer, "Composites Market Report 2019," 2019.
- [49] "Carbon Fiber Market Analysis: Industry market size, plant capacity, production, operating efficiency, Demand & Supply, end-user industries, sales channel, regional demand, foreign trade, company share, 2015-2035," *Carbon Fibre Market Size, Growth | Industry Forecast, 2035*. [Online]. Available: <https://www.chemanalyst.com/industry-report/carbon-fiber-market-676>. [Accessed: 30-May-2023].
- [50] S. Park, *Carbon Fibers*, 2nd ed. Springer Nature, 2018.
- [51] E. Fitzer, K.-H. Kochling, H. P. Boehm, and H. Marsh, "(IUPAC Recommendations 1995) Recommended terminology for description of carbon as a solid," *Pure Appl. Chem.*, vol. 67, no. 3, pp. 473–506, 1995.
- [52] J.-B. Donnet, T. W. Wang, S. Rebouillat, and J. C. M. Peng, *Carbon fibres*, 3rd ed. Marcel Dekker Inc., 1998.
- [53] E. Frank, L. M. Steudle, D. Ingildeev, J. M. Spçrl, and M. R. Buchmeiser, "Carbon Fibers : Precursor Systems , Processing , Structure , and Properties," *Angew. Rev.*, pp. 5262–5298, 2014.

- [54] J. F. Snyder, E. B. Gienger, and E. D. Wetzel, “Performance metrics for structural composites with electrochemical multifunctionality,” 2015.
- [55] M. L. Minus and S. Kumar, “The processing, properties, and structure of carbon fibers,” *Jom*, vol. 57, no. 2, pp. 52–58, 2005.
- [56] X. Huang, “Fabrication and properties of carbon fibers,” *Materials (Basel)*., vol. 2, no. 4, pp. 2369–2403, 2009.
- [57] E. Pop, V. Varshney, and A. K. Roy, “Thermal properties of graphene: Fundamentals and applications,” *MRS Bull.*, vol. 37, no. 12, pp. 1273–1281, 2012.
- [58] W. Johnson, “Structure of High Modulus Carbon Fibres,” *Nature*, vol. 215, pp. 384–396, 1967.
- [59] D. J. Johnson, “Structure-property relationships in carbon fibres,” *J. Phys. D. Appl. Phys.*, vol. 20, no. 3, pp. 286–291, 1987.
- [60] M. G. Northolt, L. H. Veldhuizen, and H. Jansen, “Tensile deformation of carbon fibers and the relationship with the modulus for shear between the basal planes,” *Carbon N. Y.*, vol. 29, no. 8, pp. 1267–1279, 1991.
- [61] O. Paris, D. Loidl, H. Peterlik, H. Lichtenegger, and P. Fratzl, “The internal structure of single carbon fibers determined by simultaneous small- and wide-angle X-ray scattering,” *J. Appl. Crystallogr.*, vol. 33, pp. 695–699, 2000.
- [62] F. Liu, H. Wang, L. Xue, L. Fan, and Z. Zhu, “Effect of microstructure on the mechanical properties of PAN-based carbon fibers during high-temperature graphitization,” *J. Mater. Sci.*, vol. 43, pp. 4316–4322, 2008.
- [63] F. Yang *et al.*, “Effect of amorphous carbon on the tensile behavior of polyacrylonitrile (PAN) -based carbon fibers,” *J. Mater. Sci.*, vol. 54, no. 11, pp. 8800–8813, 2019.
- [64] G. Fredi *et al.*, “Graphitic microstructure and performance of carbon fibre Li-ion structural battery electrodes,” *Multifunct. Mater.*, vol. 1, no. 1, p. 015003, 2018.
- [65] M. Guigon and A. Oberlin, “Microtexture and Structure of Some High-Modulus , PAN-Base Carbon Fibres,” *Fibre Sci. Technol.*, vol. 20, pp. 177–198, 1984.
- [66] M. Guigon and A. Oberlin, “Microtexture and Structure of Some High Tensile Strength , PAN-Base Carbon Fibres,” *Fibre Sci. Technol.*, vol. 20, pp. 55–72, 1984.
- [67] V. Serin, R. Fourmeaux, Y. Kihn, J. Sevely, and M. Guigon, “Nitrogen distribution in high tensile strength carbon fibres,” *Carbon N. Y.*, vol. 28, no. 4, pp. 573–578, 1990.
- [68] L. Laffont, “An EELS study of the structural and chemical transformation of PAN polymer to solid carbon,” vol. 42, pp. 2485–2494, 2004.
- [69] M. Ji, C. Wang, Y. Bai, M. Yu, and Y. Wang, “Comparison of tensile fracture

- morphologies among various polyacrylonitrile-based carbon fibers,” *Polym. Bull.*, vol. 390, pp. 381–389, 2007.
- [70] S. D. Gardner, G. He, and C. U. Pittman, “A spectroscopic examination of carbon fiber cross sections using XPS and ISS,” *Carbon N. Y.*, vol. 34, no. 10, pp. 1221–1228, 1996.
 - [71] S. Duan, F. Liu, T. Pettersson, C. Creighton, and L. E. Asp, “Determination of transverse and shear moduli of single carbon fibres,” *Carbon N. Y.*, vol. 158, pp. 772–782, 2020.
 - [72] Toray, “Types of Carbon Fiber,” 2020. [Online]. Available: <https://www.toraycma.com/page.php?id=661>. [Accessed: 30-Nov-2020].
 - [73] M. S. Dresselhaus, G. Dresselhaus, K. Sugihara, I. L. Spain, and H. A. Goldberg, *Graphite Fibers and Filaments*, vol. 5, no. 4. Berlin, Heidelberg: Springer Berlin Heidelberg, 1988.
 - [74] K. Sun, M. A. Strosio, and M. Dutta, “Graphite C-axis thermal conductivity,” *Superlattices Microstruct.*, vol. 45, no. 2, pp. 60–64, 2009.
 - [75] M. H. Kjell, E. Jacques, and D. Zenkert, “PAN-Based Carbon Fiber Negative Electrodes for Structural Lithium-Ion Batteries,” vol. 158, no. 12, pp. 1455–1460, 2011.
 - [76] S. Duan *et al.*, “Effect of lithiation on the elastic moduli of carbon fibres,” *Carbon N. Y.*, vol. 185, pp. 234–241, 2021.
 - [77] E. Jacques, M. H. Kjell, D. Zenkert, G. Lindbergh, and M. Behm, “Expansion of carbon fibres induced by lithium intercalation for structural electrode applications,” *Carbon N. Y.*, no. 59, pp. 246–254, 2013.
 - [78] E. Jacques, M. H. Kjell, D. Zenkert, G. Lindbergh, M. Behm, and M. Willgert, “Impact of electrochemical cycling on the tensile properties of carbon fibres for structural lithium-ion composite batteries,” *Compos. Sci. Technol.*, vol. 72, no. 7, pp. 792–798, 2012.
 - [79] E. Jacques *et al.*, “Impact of Mechanical loading on the electrochemical behaviour of carbon fibres for use in energy storage composite materials,” in *18th International Conference on Composite Materials*, 2011, pp. 1–6.
 - [80] M. Johansen, C. Schlueter, P. L. Tam, L. E. Asp, and F. Liu, “Mapping nitrogen heteroatoms in carbon fibres using atom probe tomography and photoelectron spectroscopy,” *Carbon N. Y.*, vol. 179, pp. 20–27, 2021.
 - [81] W. Johannisson *et al.*, “Multifunctional performance of a carbon fiber UD lamina electrode for structural batteries,” *Compos. Sci. Technol.*, vol. 168, no. August, pp. 81–87, 2018.
 - [82] M. Johansen, J. Xu, P. L. Tam, L. E. Asp, and F. Liu, “Lithiated carbon fibres for structural batteries characterised with Auger electron spectroscopy,” *Appl. Surf. Sci.*, vol. 627, no. April, p. 157323, Aug. 2023.

- [83] M. K. Miller and R. G. Forbes, *Atom probe tomography and the local electrode atom probe*. Springer, 2014.
- [84] T. F. Kelly and M. K. Miller, “Atom probe tomography,” *Rev. Sci. Instrum.*, vol. 78, no. 3, 2007.
- [85] K. Thompson, D. Lawrence, D. J. Larson, J. D. Olson, T. F. Kelly, and B. Gorman, “In situ site-specific specimen preparation for atom probe tomography,” *Ultramicroscopy*, vol. 107, no. 2–3, pp. 131–139, 2007.
- [86] J. C. Woicik, *Hard X-ray Photoelectron Spectroscopy (HAXPES)*. Springer International Publishing, 2016.
- [87] A. Jablonski and C. J. Powell, “Practical expressions for the mean escape depth, the information depth, and the effective attenuation length in Auger-electron spectroscopy and x-ray photoelectron spectroscopy,” *J. Vac. Sci. Technol. A Vacuum, Surfaces, Film.*, vol. 27, no. 2, pp. 253–261, 2009.
- [88] C. Schlueter *et al.*, “The new dedicated HAXPES beamline P22 at PETRA III,” in *AIP Conference Proceedings*, 2019, vol. 2054, no. 040010.
- [89] S. Tanuma, C. J. Powell, and D. R. Penn, “Calculations of electron inelastic mean free paths. IX. Data for 41 elemental solids over the 50 eV to 30 keV range,” *Surf. Interface Anal.*, vol. 43, no. 3, pp. 689–713, 2011.
- [90] P. J. Birdseye and D. A. Smith, “The electric field and the stress on a field-ion specimen,” *Surf. Sci.*, vol. 23, no. 1, pp. 198–210, Oct. 1970.
- [91] K. J. R. Rosman and P. D. P. Taylor, “Isotopic compositions of the elements 1997 (Technical Report),” *Pure Appl. Chem.*, vol. 70, no. 1, pp. 217–235, Jan. 1998.
- [92] M. Thuvander *et al.*, “Quantitative atom probe analysis of carbides,” *Ultramicroscopy*, vol. 111, no. 6, pp. 604–608, 2011.
- [93] M. Johansen and F. Liu, “Best Practices for Analysis of Carbon Fibers by Atom Probe Tomography,” *Microsc. Microanal.*, vol. 28, no. 4, pp. 1092–1101, 2022.
- [94] T. Schiros *et al.*, “Connecting dopant bond type with electronic structure in n-doped graphene,” *Nano Lett.*, vol. 12, no. 8, pp. 4025–4031, 2012.
- [95] D. Usachov *et al.*, “The chemistry of imperfections in N-graphene,” *Nano Lett.*, vol. 14, no. 9, pp. 4982–4988, 2014.
- [96] X. Wang *et al.*, “Atomistic origins of high rate capability and capacity of N-doped graphene for lithium storage,” *Nano Lett.*, vol. 14, no. 3, pp. 1164–1171, 2014.
- [97] F. Zheng, Y. Yang, and Q. Chen, “High lithium anodic performance of highly nitrogen-doped porous carbon prepared from a metal-organic framework,” *Nat. Commun.*, vol. 5, no. May, pp. 1–10, 2014.
- [98] B. Zhang *et al.*, “Correlation between atomic structure and electrochemical performance of anodes made from electrospun carbon nanofiber films,” *Adv.*

Energy Mater., vol. 4, no. 7, 2014.

- [99] Z. He *et al.*, “Electrospun nitrogen-doped carbon nanofiber as negative electrode for vanadium redox flow battery,” *Appl. Surf. Sci.*, vol. 469, no. September 2018, pp. 423–430, 2019.
- [100] N. Ishida, H. Fukumitsu, H. Kimura, and D. Fujita, “Direct mapping of Li distribution in electrochemically lithiated graphite anodes using scanning Auger electron microscopy,” *J. Power Sources*, vol. 248, pp. 1118–1122, 2014.
- [101] M. Hoffmann, M. Zier, S. Oswald, and J. Eckert, “Challenges for lithium species identification in complementary Auger and X-ray photoelectron spectroscopy,” *J. Power Sources*, vol. 288, pp. 434–440, 2015.
- [102] M. Hoffmann, S. Oswald, M. Zier, and J. Eckert, “Auger and X-ray photoelectron spectroscopy on lithiated HOPG,” *Surf. Interface Anal.*, vol. 48, no. 7, pp. 501–504, 2016.
- [103] S. H. Kim *et al.*, “Verification of Delayed Permanent Lithium Intercalation into Graphite Interlayers by Surface Treatment of Lithium-Ion Battery Anodes,” *J. Electrochem. Soc.*, vol. 164, no. 9, pp. A2290–A2294, 2017.
- [104] K. Kalaga, I. A. Shkrob, R. T. Haasch, C. Peebles, J. Bareño, and D. P. Abraham, “Auger Electrons as Probes for Composite Micro- and Nanostructured Materials: Application to Solid Electrolyte Interphases in Graphite and Silicon-Graphite Electrodes,” *J. Phys. Chem. C*, vol. 121, no. 42, pp. 23333–23346, 2017.
- [105] E. Y. Jung *et al.*, “Experimental study on solid electrolyte interphase of graphite electrode in Li-ion battery by surface analysis technique,” *Mol. Cryst. Liq. Cryst.*, vol. 663, no. 1, pp. 158–167, 2018.
- [106] S. Oswald, “Auger-and X-ray Photoelectron Spectroscopy at Metallic Li Material: Chemical Shifts Related to Sample Preparation, Gas Atmosphere, and Ion and Electron Beam Effects,” *Batteries*, vol. 8, no. 3, 2022.
- [107] Y. Zhang *et al.*, “Application of Auger electron spectroscopy in lithium-ion conducting oxide solid electrolytes,” *Nano Res.*, vol. 3, pp. 1–10, 2022.
- [108] R. E. Clausing, D. S. Easton, and G. L. Powell, “Auger spectra of lithium metal and lithium oxide,” *Surf. Sci.*, vol. 36, no. 1, pp. 377–379, 1973.
- [109] S. Craig, G. L. Harding, and R. Payling, “Auger lineshape analysis of carbon bonding in sputtered metal-carbon thin films,” vol. 124, pp. 591–601, 1983.
- [110] J. S. Murday, B. I. Dunlap, F. L. Hutson, and P. Oelhafen, “Carbon KVV Auger line shapes of graphite and stage-one cesium and lithium intercalated graphite,” *Phys. Rev. B*, vol. 24, no. 8, 1981.
- [111] K. Ji *et al.*, “Lithium intercalation into bilayer graphene,” *Nat. Commun.*, vol. 10, no. 1, pp. 1–10, 2019.
- [112] Y. Fang *et al.*, “Lithium insertion in hard carbon as observed by ^7Li NMR and

- XRD. The local and mesoscopic order and their relevance for lithium storage and diffusion,” *J. Mater. Chem. A*, no. 10, pp. 10069–10082, 2022.
- [113] B. J. Wicks and R. A. Coyle, “Microstructural inhomogeneity in carbon fibres,” *J. Mater. Sci.*, vol. 11, no. 2, pp. 376–383, 1976.
 - [114] S. H. Kim *et al.*, “Atom probe analysis of electrode materials for Li-ion batteries: Challenges and ways forward,” *J. Mater. Chem. A*, vol. 10, no. 9, pp. 4926–4935, 2022.
 - [115] B. Pfeiffer, J. Maier, J. Arlt, and C. Nowak, “In Situ Atom Probe Deintercalation of Lithium-Manganese-Oxide,” *Microsc. Microanal.*, vol. 23, no. 2, pp. 314–320, 2017.
 - [116] E. V Woods *et al.*, “A versatile and reproducible cryo-sample preparation methodology for atom probe studies,” pp. 1–23, Mar. 2023.
 - [117] P. Bièvre, M. Gallet, N. E. Holden, and I. L. Barnes, “Isotopic Abundances and Atomic Weights of the Elements,” *J. Phys. Chem. Ref. Data*, vol. 13, no. 3, pp. 809–891, 1984.
 - [118] M. P. Moody, L. T. Stephenson, A. V. Ceguerra, and S. P. Ringer, “Quantitative binomial distribution analyses of nanoscale like-solute atom clustering and segregation in atom probe tomography data,” *Microsc. Res. Tech.*, vol. 71, no. 7, pp. 542–550, 2008.
 - [119] A. Shariq, T. Al-Kassab, R. Kirchheim, and R. B. Schwarz, “Exploring the next neighbourhood relationship in amorphous alloys utilizing atom probe tomography,” *Ultramicroscopy*, vol. 107, no. 9, pp. 773–780, 2007.

